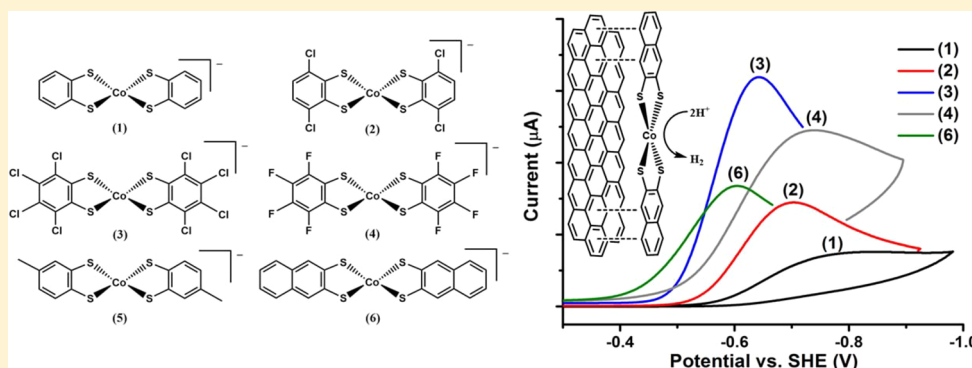


# Immobilized Cobalt Bis(benzenedithiolate) Complexes: Exceptionally Active Heterogeneous Electrocatalysts for Dihydrogen Production from Mildly Acidic Aqueous Solutions

Shawn C. Eady, Molly M. MacInnes, and Nicolai Lehnert\*<sup>✉</sup>

Department of Chemistry, University of Michigan, 930 North University Avenue, Ann Arbor, Michigan 48109, United States

## Supporting Information



**ABSTRACT:** A series of cobalt bis(benzenedithiolate) complexes with varying benzenedithiolate (general abbreviation: bdt<sup>2-</sup>) ring substitutions (S<sub>2</sub>C<sub>6</sub>X<sub>4</sub><sup>2-</sup>) were prepared and adsorbed on inexpensive electrodes composed of (a) reduced graphene oxide (RGO) electrodeposited on fluorine-doped tin oxide (FTO) and (b) highly ordered pyrolytic graphite (HOPG). The catalyst-adsorbed electrodes are characterized by X-ray photoelectron spectroscopy. Catalyst loading across the ligand series improved notably with increasing halide substitution [from 2.7 × 10<sup>-11</sup> mol cm<sup>-2</sup> for TBA[Co(S<sub>2</sub>C<sub>6</sub>H<sub>4</sub>)<sub>2</sub>] (1) to 6.22 × 10<sup>-10</sup> mol cm<sup>-2</sup> for TBA[Co(S<sub>2</sub>C<sub>6</sub>Cl<sub>4</sub>)<sub>2</sub>] (3)] and increasing ring size of the benzenedithiolate ligand [up to 3.10 × 10<sup>-9</sup> mol cm<sup>-2</sup> for TBA[Co(S<sub>2</sub>C<sub>10</sub>H<sub>6</sub>)<sub>2</sub>] (6)]. Electrochemical analysis of the complexes immobilized on HOPG elicits a reductive current response indicative of dihydrogen generation in the presence of mildly acidic aqueous solutions (pH 2–4) of trifluoroacetic acid, with overpotentials of around 0.5 V versus SHE (measured vs platinum). Rate constant (*k*<sub>obs</sub>) estimates resulting from cyclic voltammetry analysis range from 24 to 230 s<sup>-1</sup> with the maximum *k*<sub>obs</sub> for TBA[Co(S<sub>2</sub>C<sub>6</sub>H<sub>2</sub>Cl<sub>2</sub>)<sub>2</sub>] (2) at an overpotential of 0.59 V versus platinum. Controlled-potential electrolysis studies performed in 0.5 M H<sub>2</sub>SO<sub>4</sub> at -0.5 V versus SHE show impressive initial rate constants of over 500 s<sup>-1</sup> under bulk electrolysis conditions; however, steady catalyst deactivation over an 8 h period is observed, with turnover numbers reaching 9.1 × 10<sup>6</sup>. Electrolysis studies reveal that halide substitution is a central factor in improving the turnover stability, whereas the ring size is less of a factor in optimizing the long-term stability of the heterogeneous catalyst manifolds. Catalyst deactivation is likely caused by catalyst desorption from the electrode surfaces.

## INTRODUCTION

Devices capable of generating dihydrogen from a renewable energy source are crucial for meeting the global dihydrogen consumption demand in a sustainable way and for efforts to replace carbon-based fuel technologies with more sustainable alternatives.<sup>1–4</sup> Large-scale dihydrogen production from protons and electrons, whether directly coupled to water oxidation photoanodes or electrolyzers powered by renewable energy sources, must inevitably be facilitated by heterogeneous catalysts to allow for application of the catalysts in large-scale flow reactors.<sup>5–7</sup> To this end, electrocatalysts for dihydrogen production must be designed that meet the demands of these systems and, at the same time, are inexpensive and easy to assemble and that can be prepared on a large scale without difficulty. These electrocatalysts could be built either from catalytically active electrode materials or from molecular

catalysts immobilized on the electrode surfaces.<sup>7–10</sup> The latter approach has the advantage that the molecular catalysts can be improved in a systematic manner and derivatized to meet given application needs, as demonstrated in this work. However, a substantial challenge in this regard is to design suitable interfaces that allow for the easy, yet stable and affordable, attachment of the catalysts to the electrode surfaces. In this paper, we further demonstrate that reduced graphene oxide (RGO) films can serve as inexpensive, yet extremely versatile, interfaces to adsorb a variety of cobalt bis(benzenedithiolate), [Co<sup>III</sup>(bdt)<sub>2</sub>]<sup>2-</sup>, dihydrogen production catalysts to semiconductor electrode surfaces, yielding robust and highly active platforms for electrocatalytic dihydrogen generation.

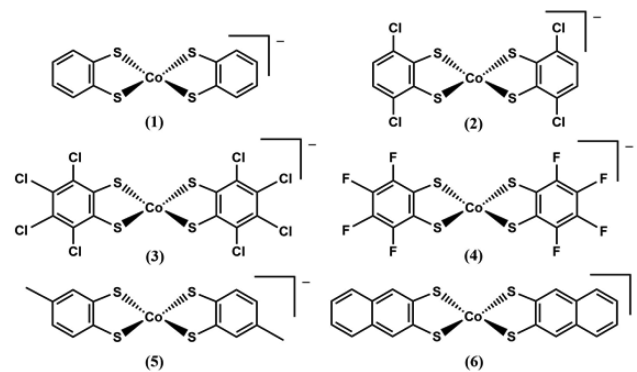
Received: June 25, 2017

In addition to the interface, fast, efficient, and inexpensive electrocatalysts are necessary to obtain platinum-free manifolds for dihydrogen production. Previous research in the renewable energy field has “unearthed” a number of inexpensive iron, nickel, and cobalt electrocatalysts for dihydrogen production.<sup>2,4,11–55</sup> Solid-state and molecular catalysts alike have displayed impressive proton reduction activity, rivaling platinum in overpotential ( $\eta$ ), turnover frequency (TOF), and turnover number (TON).<sup>46,47,56–62</sup> In some cases, these systems have nearly matched or even exceeded platinum with regard to stability in poisoning conditions or for dual catalysis applications, a milestone that should be held in high regard, considering the decades of catalyst development spent toward platinum substitution.<sup>1,46,47,63</sup> Still, the design of versatile and inexpensive heterogeneous catalyst manifolds remains a major challenge for the development of cost-efficient dihydrogen production systems.<sup>48,49,64</sup>

Cobalt(III) bis(benzenedithiolate) and corresponding cobalt(III) bis(dithiolene) complexes, discovered nearly 5 decades ago, have historically been researched for various applications based on their strong absorption features and unique electronic structures.<sup>26,27,50,65–76</sup> Recently, these complexes have been found to be active for dihydrogen production in acidic organic solutions by McNamara et al., with a maximum TOF of 3400 h<sup>-1</sup> and a TON of 9000 in 12 h in solution.<sup>26,27</sup> Later, we reported adsorption of a molecular cobalt bis(benzenedithiolate) species onto graphitic supports to provide a heterogeneous proton reduction system with high activity from mildly acidic aqueous solutions.<sup>77</sup> In parallel studies, these catalyst systems have also been investigated as two-dimensional polymer materials on graphitic supports, as well as one-dimensional light-permeable materials on silicon surfaces for photoelectrocatalysis.<sup>67,68</sup> Curiously, these heterogeneous manifolds, whether prepared directly by the adsorption of molecular catalysts onto a support or designed from a polymer material transferred to a surface, show substantially higher TOFs than the corresponding catalysts in homogeneous phase. As demonstrated in this work, cobalt bis(benzenedithiolate) based heterogeneous catalyst manifolds approach even the catalytic activities of nickel bis(diphosphine) systems (albeit under different conditions), which have become the gold standard for homogeneous and heterogeneous dihydrogen production systems in a number of applications.<sup>19,46,47,49,78</sup> Moreover, cobalt bis(benzenedithiolate) complexes provide versatility for incorporation into devices because both the graphitic supports (e.g., graphene and RGO) used to adsorb these complexes and their polymeric forms can be immobilized on a variety of electrode materials. While the polymeric systems potentially offer more variety in the choice of electrode materials, one challenge with such materials is functionalization and thereby the systematic improvement of their catalytic performance. For this reason, investigation of the molecular catalysts, which are easily derivatized, is of great interest to determine the effects of varying the functionality on the overall performance of the immobilized cobalt bis(benzenedithiolate) systems, which is the key point of this study.

Herein, we report a series of cobalt bis(benzenedithiolene) derivatives (Chart 1) adsorbed onto graphitic surfaces and investigations into their dihydrogen production activity in acidic aqueous solutions, including the quantification of catalyst loadings and activity data. Because of the ease of preparation and potential future applications of these systems, initial studies

Chart 1. Cobalt Bis(benzenedithiolate) Derivatives



were conducted on RGO electrodeposited on fluorine-doped tin oxide (FTO), which provides a design strategy of how these catalysts could be immobilized on a variety of supports, especially semiconductor electrodes, using RGO as the universal interface. Quantitative comparisons, based on this approach, are hampered by the fact that consistency in the RGO coverage and topography is generally low and there is a lack of stability of the FTO electrodes at low pH. To complement these tests, the catalysts were also adsorbed on highly ordered pyrolytic graphite (HOPG) electrodes. HOPG electrodes provide a more consistent surface area and topography, therefore allowing for a quantitative comparison between different catalyst derivatives in the surface-immobilized state. The resulting series of heterogeneous electrocatalysts provides detailed insight into the effect of benzenedithiolate ligand substitution on the surface adsorption and coverage, electrocatalytic activity, and lifetime of the catalysts, allowing us to optimize the catalytic properties of these complexes.

## EXPERIMENTAL SECTION

**General Methods.** Chemicals were of the highest purity grade commercially available and were used without further purification (unless mentioned). Methanol (anhydrous, ACS grade) was purchased from Fisher, distilled over calcium hydride, and then degassed via extended dinitrogen purges prior to use. Acetonitrile (ACS grade), sodium methoxide, trifluoroacetic acid (TFA), sulfuric acid, potassium ferricyanide, and potassium ferrocyanide were purchased from Fisher. 1,2-Benzenedithiol, toluene-3,4-dithiol, and 3,6-dichloro-1,2-benzenedithiol were purchased from Sigma and used without further purification. Graphite powder was purchased from MTI Corp. All procedures were performed under a dinitrogen atmosphere unless otherwise specified.

**Preparation of Dithiol Ligand Derivatives.** Tetrahalidedithiol ligands were prepared using a slightly modified method from that reported by Gray and co-workers.<sup>65</sup> Naphthalenedithiol was prepared by first following procedures reported by Hart et al. to give *o*-dibromonaphthalene, followed by alkylthiol formation and alkyl cleavage as outlined by Montanucci and co-workers.<sup>79,80</sup>

**3,4,5,6-Tetrachlorobenzenedithiol.** A mixture of hexachlorobenzene (1 g, 3.5 mmol), sodium hydrogen sulfide (0.75 g, 13 mmol), sulfur (0.08 g, 2.5 mmol), and iron powder (0.18 g, 3.2 mmol) was heated in 50 mL of *N,N*-dimethylformamide at 140 °C for 8 h. After cooling, 100 mL of distilled water was added, and the mixture was allowed to briefly stir at room temperature, during which time a black precipitate formed. The precipitate was filtered off, washed with water, and then dried in vacuo. The dried solid was added to a suspension of zinc oxide in a 1:1 methanol/1 M aqueous sodium hydroxide solution, which was refluxed for 1 h. After cooling, the mixture was filtered, and the yellow filtrate was acidified with a 1 M HCl solution to precipitate the dithiol product. The solid was dried and recrystallized from benzene to afford 3,4,5,6-tetrachlorobenzenedithiol 0.44 g (45% yield)

as a pale-yellow powder.  $^1\text{H NMR}$  (400 MHz,  $\text{CD}_2\text{Cl}_2$ ):  $\delta_{\text{H}}$  4.79 (s, 2H).

**3,4,5,6-Tetrafluorobenzenedithiol.** A mixture of 1,2-dibromo-3,4,5,6-tetrafluorobenzene (1 g, 3.2 mmol), sodium hydrogen sulfide (0.75 g, 13 mmol), sulfur (0.08 g, 2.5 mmol), and iron powder (0.18 g, 3.2 mmol) was heated in 50 mL of *N,N*-dimethylformamide at 120 °C for 8 h. After cooling, 100 mL of distilled water was added, and the mixture was allowed to briefly stir at room temperature, during which time a black precipitate formed. The precipitate was filtered off, washed with water, and then dried in vacuo. The dried solid was added to a suspension of zinc oxide in a 1:1 methanol/1 M aqueous sodium hydroxide solution, which was refluxed for 1 h. After cooling, the mixture was filtered, and the yellow filtrate was acidified with a 1 M HCl solution to precipitate the dithiol product. The solid was dried and recrystallized from benzene to afford 0.12 g (17% yield) of 3,4,5,6-tetrafluorobenzenedithiol as a pale-yellow powder.  $^1\text{H NMR}$  (400 MHz,  $\text{CD}_2\text{Cl}_2$ ):  $\delta_{\text{H}}$  4.03 (s, 2H).

**6,7-Dibromo-1,4-dihydronaphthalene-1,4-epoxide.** To a stirred solution of 1,2,4,5-tetrabromobenzene (8 g, 20 mmol) and furan (10 mL) in dry toluene (200 mL) at  $-23$  °C under argon was added dropwise over 3 h *n*-BuLi (22 mmol in 200 mL of hexane). After the mixture slowly warmed to room temperature, methanol (1 mL) was added, the mixture was washed with water and dried, and the solvent was removed (rotavap). The resulting yellow oily solid was triturated with hexane to give an off-white solid. This crude product was chromatographed on silica gel using dichloromethane/hexane (1:1) as the eluent to give 0.7 g (74% yield) of 6,7-dibromo-1,4-dihydronaphthalene-1,4-epoxide as a white powder.  $^1\text{H NMR}$  (400 MHz,  $\text{CD}_2\text{Cl}_2$ ):  $\delta_{\text{H}}$  5.62 (s, 2H), 6.95 (s, 2H), 7.44 (s, 2H).

**1,2-Dibromonaphthalene.** A suspension of zinc powder (2 g) in 60 mM dry tetrahydrofuran (THF) under a dinitrogen atmosphere was cooled to 0 °C. Titanium tetrachloride (2 mL) was added dropwise, and the mixture was heated to reflux for 30 min. The reaction was then again cooled to 0 °C, and a solution of 6,7-dibromo-1,4-dihydronaphthalene-1,4-epoxide (1.0 g, 3.3 mmol) in 20 mL of THF was added dropwise. The mixture was refluxed overnight, cooled, and poured into 100 mL of cold 10% HCl. The mixture was extracted with dichloromethane, washed with water, dried with sodium sulfate, and reduced in vacuo to an off-white powder. The crude product was chromatographed on silica gel using dichloromethane/hexane (1:1) as the eluent to afford 0.7 g (74% yield) of 1,2-dibromonaphthalene as a white powder.  $^1\text{H NMR}$  (400 MHz,  $\text{CD}_2\text{Cl}_2$ ):  $\delta_{\text{H}}$  8.15 (s, 2H), 7.75 (m, 2H), 7.5 (m, 2H).

**1,2-Naphthalenedithiol.** A solution of 1,2-dibromonaphthalene (1 g, 3.5 mmol) and sodium propanethiolate (1.7 g, 17.5 mmol) in 50 mL of *N,N*-dimethylacetamide was stirred under a dinitrogen atmosphere at 100 °C for 12 h. Sodium metal (0.6 g, 26 mmol) was cut into small pieces and added to the solution, which was allowed to continue stirring at 100 °C for 12 h. The resulting mixture was poured into 100 mL of a 0.1 M HCl solution and subsequently extracted three times with ether. The combined organic layer was washed with water, dried with sodium sulfate, and reduced in vacuo to give 0.6 g (89% yield) of 1,2-naphthalenedithiol as a yellow solid.  $^1\text{H NMR}$  (400 MHz,  $\text{CD}_2\text{Cl}_2$ ):  $\delta_{\text{H}}$  7.9 (s, 2H), 7.42 (m, 2H), 6.64 (m, 2H), 3.95 (s, 2H).

**Preparation of Cobalt Bis(benzenedithiolate) Derivatives.** The general procedure for the synthesis of cobalt bis(benzenedithiolene) complexes is based on the procedure reported by Gray and co-workers:<sup>65</sup>

In a dinitrogen atmosphere glovebox, a solution of the dithiol ligand (2.05 mmol) and sodium methoxide (0.23 g, 4.10 mmol) is added dropwise to a suspension of cobalt(II) sulfate hexahydrate (1 mmol) in 30 mL of dry methanol, and the resulting solution is stirred for 2 h. A solution of tetrabutylammonium bromide (1.05 mmol) in 5 mL of methanol is added at this time, and the solution is stirred for an additional 2 h. The solvent volume is reduced by vacuum to <10 mL, giving a precipitate, which is filtered off, washed with methanol, and dried. Recrystallization of the solid from dichloromethane/ether yields the cobalt bis(benzenedithiolate) complexes as dark blue-black microcrystalline solids.

**Tetrabutylammonium Cobalt Bis(benzenedithiolate) (1).** Recrystallization of the solid from dichloromethane/ether yielded (TBA)-[Co( $\text{S}_2\text{C}_6\text{H}_4$ )<sub>2</sub>] as a dark-blue crystalline solid in 79% yield (0.460 g). Elem anal. Calcd: C, 57.80; H, 7.62; N, 2.41. Found: C, 58.10; H, 7.69; N, 2.42. ESI-MS:  $m/z$  339.9 (expected), 338.9 (found). The spectroscopic data of the product (see Figure S1) match those available in the literature.<sup>27</sup>

**Tetrabutylammonium Cobalt Bis(3,6-dichlorobenzenedithiolate) (2).** Recrystallization of the solid from dichloromethane/ether yielded (TBA)[Co( $\text{S}_2\text{C}_6\text{H}_2\text{Cl}_2$ )<sub>2</sub>] as a dark-blue crystalline solid in 64% yield (0.462 g). Elem anal. Calcd ( $\text{CH}_2\text{Cl}_2$   $1/4$  lattice occupancy): C, 45.80; H, 5.47; N, 1.89. Found: C, 45.73; H, 5.58; N, 1.91. ESI-MS:  $m/z$  477.7 (expected), 476.7 (found). The spectroscopic data of the product (see Figure S1) match those available in the literature.<sup>27</sup>

**Tetrabutylammonium Cobalt Bis(3,4,5,6-tetrachlorobenzenedithiolate) (3).** Recrystallization of the solid from dichloromethane/ether yielded (TBA)[Co( $\text{S}_2\text{C}_6\text{Cl}_4$ )<sub>2</sub>] as a dark-blue-black solid in 28% yield (0.06 g). Elem anal. Calcd: C, 39.22; H, 4.23; N, 1.63. Found: C, 40.23; H, 4.49; N, 1.62. ESI-MS:  $m/z$  615.5 (expected), 614.5 (found).

**Tetrabutylammonium Cobalt Bis(3,4,5,6-tetrafluorobenzenedithiolate) (4).** Recrystallization of the solid from dichloromethane/ether yielded (TBA)[Co( $\text{S}_2\text{C}_6\text{F}_4$ )<sub>2</sub>] as a dark-blue-black solid in 22% yield. ESI-MS:  $m/z$  483.9 (expected), 483.1 (found).

**Tetrabutylammonium Cobalt Bis(toluenedithiolate) (5).** Recrystallization of the solid from dichloromethane/ether yielded (TBA)-[Co( $\text{S}_2\text{C}_7\text{H}_7$ )<sub>2</sub>] as a dark-blue crystalline solid in 69% yield (0.420 g). Elem anal. Calcd: C, 59.08; H, 7.93; N, 2.30. Found: C, 58.83; H, 7.97; N, 2.35. ESI-MS:  $m/z$  366.9 (expected), 366.9 (found). The spectroscopic data of the product (see Figure S1) match those available in the literature.<sup>27</sup>

**Tetrabutylammonium Cobalt Bis(naphthalenedithiolate) (6).** Recrystallization of the solid from dichloromethane/ether yielded (TBA)[Co( $\text{S}_2\text{C}_{10}\text{H}_6$ )<sub>2</sub>] as a dark-blue-black crystalline solid in 29% yield (0.1 g). Crystals suitable for X-ray analysis were obtained by layering of ether on a dilute solution of **6** in dichloromethane. Elem anal. Calcd ( $\text{CH}_2\text{Cl}_2$   $1/4$  lattice occupancy): C, 61.91; H, 6.90; N, 1.99. Found: C, 62.25; H, 7.03; N, 2.02. ESI-MS:  $m/z$  438.9 (expected), 438.9 (found).

**Graphene Oxide (GO).** GO for graphene depositions was prepared via Hummer's method:<sup>81</sup>

Sodium nitrate (0.5 g) was added to 23 mL of sulfuric acid in a large beaker and stirred until dissolved. Next, 1 g of graphite powder was added and stirred. After cooling in an ice bath, potassium permanganate (3 g) was slowly added to the suspension, instigating gas formation. The ice bath was then removed, and the temperature of the suspension was brought up to room temperature. The reaction beaker was then placed in an oil bath at 40 °C and stirred for 1 h. The reaction was quenched with the slow addition of 40 mL of deionized water, causing gas production of brown vapors. After gas production ceased, the suspension was then further diluted with 40 mL of a 10%  $\text{H}_2\text{O}_2$  solution to convert the remaining manganese oxides into inert sulfates, causing a change of the solution to a brown color. The mixture was centrifuged, and the solids were washed extensively with a mixture of 5%  $\text{H}_2\text{SO}_4$  and 5%  $\text{H}_2\text{O}_2$ . The remaining powder was then washed with deionized water until neutral pH was reached. The resulting GO powder was dried in a vacuum oven at 40 °C to give 1.76 g of GO.

**RG0 Electrode Preparation.** A total of 0.5 g of GO (prepared as described above) was added to 30 mL of a 0.1 M sodium carbonate/bicarbonate buffered solution (pH 9.2) in Millipore water. The solution was stirred extensively for a long time to allow for better GO sheet separation, becoming more viscous over time. Before deposition, FTO-coated glass was cleaned by sonication in acetone, ethanol, and water. The GO solution was degassed by a purge with argon gas prior to deposition. For all depositions, the cleaned FTO-coated glass piece was used as the working electrode in the GO solution, with a platinum auxiliary electrode and a Ag/AgCl reference electrode. In a typical deposition, CV would be initiated at the open-circuit potential ( $\sim 0$  V) and scanned cathodically to  $-1.4$  V, with two cathodic scans for all graphene surfaces used for analysis here. After deposition, the surfaces

were rinsed with deionized water to remove any loose GO from the surface.

**Catalyst-Adsorbed Electrode Preparation.** All catalyst-adsorbed electrode surfaces reported in this work were prepared by soaking the graphitic electrode surfaces (FTO/RGO and HOPG) in saturated acetonitrile solutions of the cobalt bis(benzenedithiolate) complexes for 24 h. After this period, surfaces were extensively rinsed with fresh acetonitrile, acetone, and water. In addition, the surfaces were electrochemically polished by cycling from 0 to  $-1$  V to ensure that any loosely bound catalyst was sufficiently removed prior to electrochemical and X-ray photoelectron spectroscopy (XPS) analysis.

**UV–Visible Spectroscopy.** Electronic absorption spectra were collected at room temperature using an Analytic Jena Specord S600 spectrometer with a WinASPECT (V2.2) interface.

**Gas Chromatography.** Dihydrogen quantification for determination of Faradaic efficiencies was performed by direct syringe injection of the cell's atmosphere into a Trace 1310 Thermo Scientific gas chromatograph equipped with a thermal conductivity detector and a flame ionization detector as well as Supelco columns. Dihydrogen in dinitrogen mixed gases for calibration were purchased from MESA Specialty Gas.

**Electrochemical Measurements.** All electrochemical measurements were conducted in 18.2 Millipore water. Cyclic voltammetry (CV) and controlled-potential coulometry were carried out using a CHI600 electrochemical analyzer. For RGO measurements, the working electrode was a piece of FTO-coated glass (purchased from Pilkington) with thin layers of RGO electrodeposited on the surface by the method described above. Testing on FTO/RGO surfaces was performed in triplicate to ensure that no major deviation in the results due to differences in the RGO coverage occurred. For graphite measurements, an edge-plane highly ordered pyrolytic graphite electrode (HOPG; purchased from Pine Instruments) was used. A platinum wire (CH Instruments) was used as the counter electrode in all voltammetry experiments, and the reference was an aqueous Ag/AgCl electrode (CH Instruments; saturated AgCl and a KCl fill solution). All potentials are reported versus the standard hydrogen electrode (SHE) by adding 0.205 V to the potential versus Ag/AgCl/sat. KCl. Bulk electrolysis experiments were conducted in a two-compartment cell separated by a frit with the same working and reference electrodes previously mentioned and a carbon felt counter electrode (purchased from Alfa Aesar). To maintain a steady pH and provide a more consistent activity profile during electrolysis, the pH was monitored and adjusted back to the starting pH after increasing by more than 0.03 units. All solutions were prepared with a 0.1 M potassium hexafluorophosphate supporting electrolyte, purchased from Fisher, and subsequently recrystallized. Argon gas was used to deoxygenate all solutions for a minimum of 30 min prior to data collection. After every compound was tested on the HOPG electrode, the electrode was polished until no trace of catalyst activity was observed in a pH 1.5 sulfuric acid solution and then soaked in the next catalyst's soaking solution. The only exception is the bulk electrolysis of **1**, where a different electrode was used because of the fact that the previous electrode was spent from extensive polishing.

**XPS.** All XPS spectra were acquired with a Kratos Axis Ultra analyzer using an Al  $K\alpha$  (1486.6 eV) source with a monochromator. Spectra were recorded without charge neutralization at a base pressure of  $<2.5 \times 10^{-9}$  Torr. A 8 mA emission current and 14 kV anode HT were used. Survey scans were acquired at a pass energy of 160 eV. Because of the low level of catalyst loading, high-resolution XP spectra of C 1s, Co 2p, Cl 2p, and S 2p recorded at a pass energy of 20 eV provided very low signals that were difficult to visualize. For this reason, lower-resolution data recorded at a pass energy of 160 eV are shown here. The binding energies of all spectra were corrected by using the difference between the observed C 1s peak energy and the peak energy of adventitious carbon (284.6 eV).<sup>82</sup> Spectra were fit with a Shirley-type background using the CASAXPS software version 2.313. Co 2p, Cl 2p, and S 2p spectra were fit using 45% Gaussian and 55% Lorentzian line shapes. The full width at half-maximum was constrained between 0.6 and 3.0 eV for Cl 2p and S 2p spectra and

between 0.6 and 5.0 eV for Co 2p spectra. Additional peaks necessary to fit all spectra used the same fitting parameters.

**X-ray Crystallography. Structural Determination of  $[(C_4H_9)_4N][Co(S_2C_{10}H_6)_2]$  (**6**).** Blue plates of **6** were grown from a dichloromethane solution of the compound layered with diethyl ether at 22 °C. A crystal of dimensions  $0.09 \times 0.03 \times 0.01$  mm was mounted on a Rigaku AFC10K Saturn 944+ CCD-based X-ray diffractometer equipped with a low-temperature device and a Micromax-007HF copper-target microfocus rotating anode ( $\lambda = 1.54187$  Å) operated at 1.2 kW power (40 kV, 30 mA). The X-ray intensities were measured at 85(1) K with the detector placed at a distance of 42.00 mm from the crystal. A total of 2028 images were collected with an oscillation width of  $1.0^\circ$  in  $\omega$ . The exposure times were 15 s for the low-angle images and 120 s for the high-angle images. Rigaku d\*trek images were exported to *CrysAlisPro* for processing and corrected for absorption. Integration of the data yielded a total of 25589 reflections to a maximum  $2\theta$  value of  $139.28^\circ$ , of which 3213 were independent and 2640 were greater than  $2\sigma(I)$ . The final cell constants (Table S1) were based on the xyz centroids of 5786 reflections above  $10\sigma(I)$ . Analysis of the data showed negligible decay during data collection. The structure was solved and refined with the Bruker *SHELXTL* (version 2014/6) software package, using the space group  $C2/c$  with  $Z = 4$  for the formula  $C_{36}H_{48}NS_4Co$ . The cobalt dithiolate complex lies on an inversion center of the crystal lattice. The tetrabutylammonium cation lies on a 2-fold axis. All non-hydrogen atoms were refined anisotropically, with the hydrogen atoms placed in idealized positions. Full-matrix least-squares refinement based on  $F^2$  converged at  $R1 = 0.0806$  and  $wR2 = 0.2126$  based on  $I > 2\sigma(I)$  and  $R1 = 0.0949$  and  $wR2 = 0.2567$  for all data. Additional details are presented in Table S1 and are given as Supporting Information.

## RESULTS

**Syntheses and Crystal Structure.** The cobalt bis(benzenedithiolate) complexes **1–6** (general formula:  $[Co^{III}(bdt)_2]^-$ ) were all synthesized using the same general procedure originally reported by Gray and co-workers,<sup>65</sup> combining a cobalt(II) source with the dithiolate reagent in the presence of a base (sodium methoxide) and a counterion source to give the anionic cobalt(III) species as the tetrabutylammonium salts. The microcrystalline products were then characterized by mass spectrometry (MS), elemental analysis, and UV–visible spectroscopy, in addition to the crystallographic characterization for **6**.

The complexes all have strong absorption features in the near-UV ( $\sim 400$  nm) and between 500 and 700 nm, with extinction coefficients as high as 20000 and 14000  $M^{-1} cm^{-1}$ , respectively, as shown in Figure S1. The crystal structure of **6** (Figure 1) confirms the expected square-planar structure observed in other examples of cobalt bis(benzenedithiolate) complexes, with a perfectly planar structure essentially giving the molecule the “thickness” of the cobalt diameter. The packing of the molecules in the crystal shows layers of the flat molecules with completely eclipsed rings, separated by slightly offset cations, with a distance of 8.3 Å between the sandwiched cobalt bis(benzenedithiolate) molecules.

**Electrode Surface Immobilization.** XPS analysis of FTO surfaces before and after RGO electrodeposition was reported in our previous work<sup>77</sup> and reflects the change in the carbon signal in the C 1s core spectrum from having only adventitious carbon on FTO to containing a variety of C–C and  $CO_x$  species after RGO deposition. After soaking of the FTO/RGO electrodes in catalyst solutions, XPS analysis of **3** and **6** adsorbed to FTO/RGO surfaces was performed at a pass energy of 20 eV to yield high-resolution spectra. However, the substantially lower loading in these adsorbed catalyst systems ( $\sim 10^{-10}$  mol<sub>Co</sub> cm<sup>-2</sup>) compared to those in the polymeric

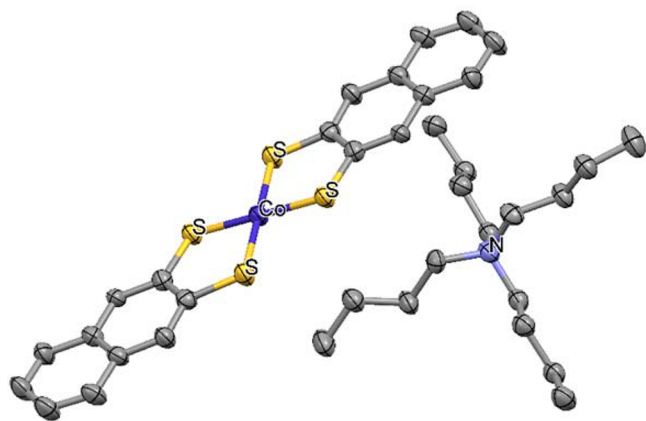


**Figure 1.** Crystal structure of (TBA)[Co(S<sub>2</sub>C<sub>10</sub>H<sub>6</sub>)<sub>2</sub>] (**6**) with ellipsoids shown at 50% probability. Hydrogen atoms are omitted for clarity. Selected bond distances [Å] and angles [deg]: Co–S 2.171(9), S–C 1.764(5), Co–N 6.45(6); S–Co–S 91.68(4).

systems ( $10^{-7}$ – $10^{-6}$  mol<sub>Co</sub> cm<sup>-2</sup>)<sup>67,68</sup> made high-resolution XPS less effective because the intensities were generally too low to distinguish energy differences that would result from the higher resolution, and often only trace signals were observed, if any at all.<sup>67,68</sup> To better visualize the features present in the spectra, data were collected at a pass energy of 160 eV. The data generally show two new features in the Co 2p core spectra, comprising two sets of Co 2p<sub>1/2</sub> and 2p<sub>3/2</sub> signals (Figures S2b and S3b). These signals have been attributed to the [Co<sup>III</sup>(bdt)<sub>2</sub>]<sup>-</sup> (778 and 794.1 eV) and [Co<sup>II</sup>(bdt\*)(bdt)]<sup>-</sup> (781 and 795 eV) resonance structures reported for cobalt bis(benzenedithiolate) complexes.<sup>66</sup> These results are also consistent with those reported for both linear and extended polymer systems of [Co(bdt)<sub>2</sub>]<sup>-</sup>.<sup>67,68</sup> The S 2p core spectrum also shows a new signal at 163 eV (Figures S2f and S3d), which is approximately at a 1.5 eV higher binding energy compared to CoS materials and consistent with XPS data of phenylthiols previously reported in the literature.<sup>83,84</sup> Analysis of **3** on FTO/RGO shows similar results for the Co 2p and S 2p spectra, in addition to showing a new signal for Cl 2p at 201 eV (Figure S2d), which is in agreement with previous literature reports for chloro-substituted ring systems.<sup>85</sup> These results (especially the unique, split cobalt XPS signals) directly confirm the molecular nature of the complexes in the surface-bound state.

**Cyclic Voltammetry (CV).** Analysis of our cobalt bis(benzenedithiolate) complexes on FTO/RGO surfaces by CV shows redox features in the range of -0.22 to -0.28 V versus SHE, as shown in Table 1. The features persist upon extended cycling, indicating the stability of the adsorbed species on the electrode surface. The redox events generally appear quasi-reversible in nature, with a higher cathodic current response than anodic ( $i_{pc}/i_{pa}$  values generally below 0.9) and further decreasing with increasing scan rate for most complexes. Peak separation was also seen to vary between species, ranging from just over 0.12 V for **4** to nearly 0.25 V for **6** (Figures S14 and S21, respectively). Most of the complexes on the FTO/RGO surfaces have  $E_{pc}$  and  $E_{pa}$  values that shift slightly with varying scan rate; however, both this phenomenon and the deviation in peak separation from the expected reversible value (0.057 V) are also observed for the ferricyanide internal standard, suggesting that this is inherent to the experimental conditions, likely caused by slow electron transfer across the FTO/RGO interface, and cannot be attributed to the adsorbed catalysts.

CV analysis of the complexes on HOPG electrodes shows redox features ranging from -0.33 to -0.57 V, consistently giving more negative  $E_{1/2}$  values compared to the corresponding species on FTO/RGO surfaces. Peak anodic/cathodic current ratios are close to 1 ( $\pm 0.1$ ) for complexes on HOPG, while a disproportionate increase of the cathodic current compared to the anodic current with increasing scan rate is still evident for all complexes with the exception of **4**. As seen for complex **6** in Figure 2, anodic and cathodic peak separations range from 0.2 to 0.3 V, which is generally consistent with the peak separation of the ferricyanide internal standard with the HOPG electrodes.

Quantification of the complex loading was performed via integration of the cathodic current response at 50 mV s<sup>-1</sup> in a pH 7, 0.1 M KPF<sub>6</sub> solution by directly attributing all passed charges to the one-electron reduction of the cobalt(III) species. This method gives a range of catalyst concentrations from  $2.70 \times 10^{-11}$  mol cm<sup>-2</sup> for **1** to  $3.10 \times 10^{-9}$  mol cm<sup>-2</sup> for **6** on HOPG. While quantitatively not highly accurate, these estimates, when taken on the same HOPG electrode for very similar types of complexes, allow for precise comparisons between catalyst derivatives and thus can inform on the effect of the ligand system on relative catalyst adsorption. Particularly interesting are the effects of increasing halide substitution of the benzenedithiolate ligand. Our CV data in Table 1 show a clear increase in the catalyst loading from **1** to **2** and **3**. The

**Table 1. Redox Potentials (vs SHE) and Selected Catalytic Properties of the Immobilized Cobalt Complexes**

complex	$E_{1/2}^{RGO,HOPG}$ (V)	$E_{cat/2}^{RGO,HOPG}$ (V)	[cat] <sub>HOPG</sub> (mol <sub>Co</sub> cm <sup>-2</sup> ) <sup>a</sup>	$\eta_{RGO,HOPG}$ (V) <sup>c</sup>	$i_{cat}$ ( $\mu$ A) <sup>d</sup>	$k_{obs}$ (s <sup>-1</sup> ) <sup>e</sup>	TOF (s <sup>-1</sup> ) <sup>f</sup>	TON (time)
Co(bdt) <sub>2</sub> ( <b>1</b> )	-0.28, -0.57	-0.65, -0.71	$2.70 \times 10^{-11b}$	0.57, 0.63	224	220	800	$4.30 \times 10^6$ (1.5 h)
Co(dcbdt) <sub>2</sub> ( <b>2</b> )	-0.25, -0.52	-0.61, -0.67	$2.60 \times 10^{-10}$	0.53, 0.59	2279	230	320	$9.10 \times 10^6$ (8 h)
Co(tcdbdt) <sub>2</sub> ( <b>3</b> )	-0.25, -0.35	-0.58, -0.52	$6.22 \times 10^{-10}$	0.5, 0.44	2818	120	140	$4.02 \times 10^6$ (8 h)
Co(tfbdtd) <sub>2</sub> ( <b>4</b> )	-0.22, -0.33	-0.57, -0.54	$1.82 \times 10^{-9}$	0.49, 0.46	2952	42	n/a	n/a
Co(tdt) <sub>2</sub> ( <b>5</b> )	-0.28, -0.45	n/a	$1.45 \times 10^{-9}$	n/a	n/a	n/a	n/a	n/a
Co(ndt) <sub>2</sub> ( <b>6</b> )	-0.24, -0.46	n/a, -0.59	$3.10 \times 10^{-9}$	n/a, 0.51	2906	24	4	$7.90 \times 10^3$ (1 h)

<sup>a</sup>Determined by integration of the cathodic current response in cyclic voltammograms of HOPG/catalyst electrodes at 50 mV s<sup>-1</sup> scan rate, based on an HOPG electrode area of 0.2 cm<sup>2</sup>. <sup>b</sup>Loading determined from CV experiments. CPE experiments for **1** were performed with a different HOPG electrode because of damage to the first electrode, with a measured loading of  $4.04 \times 10^{-11}$  mol<sub>Co</sub> cm<sup>-2</sup>. <sup>c</sup>Overpotential determined by comparison of the half-wave potential ( $E_{cat/2}$ ) with the open-circuit potential of platinum in the same 1 mM TFA solution under 1 atm of dihydrogen (Figure S13). <sup>d</sup>Peak catalytic current observed at pH 1.5 (or at activity saturation pH if higher) on an HOPG electrode. <sup>e</sup>Calculated from CV data by the use of eq 1 with  $i_{cat}$  determined at a scan rate of 50 mV s<sup>-1</sup> at 298 K and pH 1.5 (on HOPG). <sup>f</sup>Average TOF from CPE experiments (at pH 0.3), determined based on the total charge passed prior to reaching the plateau current (TON time), divided by the reductive equivalents for dihydrogen formation (2) and the total amount of catalyst present on the electrode surface.

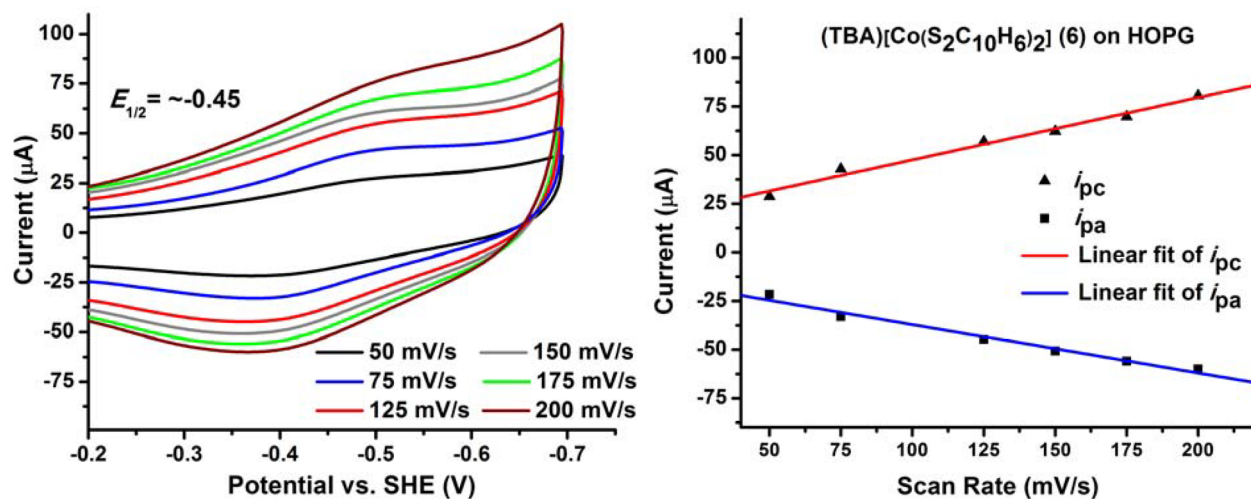


Figure 2. Left: CV of 6 adsorbed on an HOPG working electrode in an aqueous 0.1 M  $\text{KPF}_6$  solution at varying scan rates. Right: Plot of the cathodic and anodic peak heights as a function of the scan rate. Platinum counter and Ag/AgCl reference electrodes were used, and potentials are reported versus SHE.

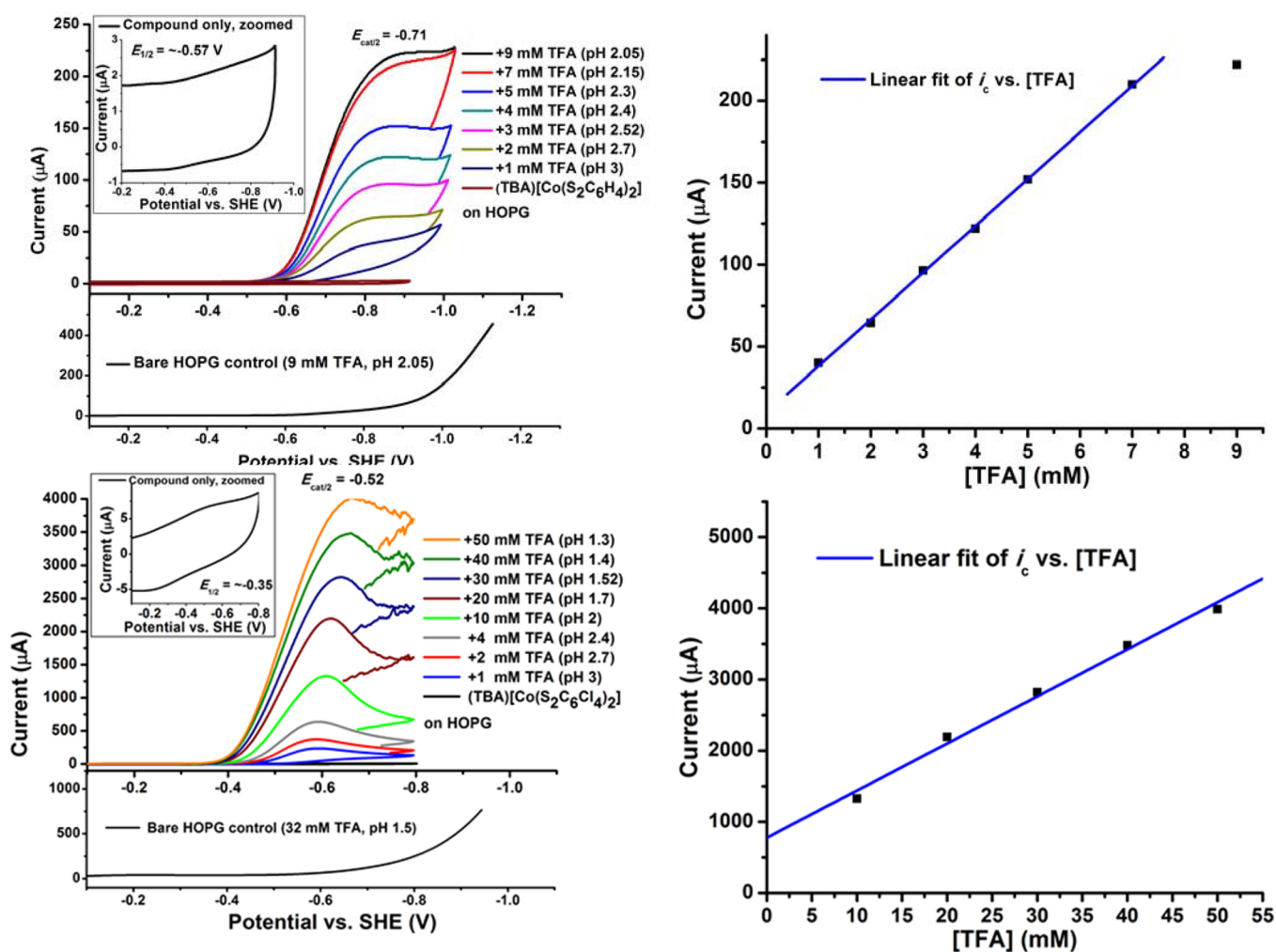


Figure 3. CV plots of 1 (top left) and 3 (bottom left) adsorbed on an HOPG working electrode in an aqueous 0.1 M  $\text{KPF}_6$  solution with the addition of TFA at a scan rate of 50  $\text{mV s}^{-1}$ . The current response of the bare HOPG electrode in a TFA solution is displayed in the lower panels, and the inset provides a zoomed view of the catalyst-adsorbed electrode in the absence of acid. The corresponding plots of peak catalytic current versus acid concentration are presented for 1 (top right) and 3 (bottom right). Platinum counter and Ag/AgCl reference electrodes were used, and potentials are reported versus SHE.

tetrafluoro-substituted complex **4** is observed to approximately double the loading in comparison to the tetrachloro-substituted species. A comparison of the benzene and naphthalene ring systems for complexes **1** and **6** shows a substantial increase in the catalyst loading for **6**, with about 2 orders of magnitude higher loading for the larger ring system (Table 1). A 50-fold increase in the catalyst loading is observed from **1** to the toluenedithiolate derivative, **5**, indicating that electron-donating substituents on the ligand ring system can also improve adsorption. On the basis of these results alone, complex **6** with the naphthalenedithiolate ligand is the best catalyst for adsorption on graphitic surfaces, resulting in the best surface coverage.

**Electrocatalytic Studies.** For all complexes adsorbed on FTO/RGO electrodes, the addition of TFA to the aqueous solutions resulted in an increase in the cathodic current coinciding with the disappearance of the anodic wave, indicative of proton reduction at the electrode surface. The complexes consistently required a pH lower than 4 to show an increase in the current response (the exact pH at which the current increases varies between 3 and 4 depending on the applied complex). The current response increases linearly with further addition of acid except in the cases of **5** and **6**, which stopped increasing and subsequently decreased to the background current upon further acid addition (Figures S19 and S22). In some of the repeated trials, even the initial current increase was absent for **5** and **6** upon acid addition, and the original redox feature was no longer observed, suggesting catalyst desorption or decomposition. Previous results indicate that the catalysts simply desorb from the surface over time and that this is the main reason for the loss of activity.<sup>86</sup> For complexes **1–4**, activity saturation was not observed up to a TFA concentration of 2 mM (pH 2.7). Note that below this pH, the FTO electrodes are not cathodically durable for testing.<sup>77</sup>  $E_{\text{cat}/2}$  values at this pH range from  $-0.57$  to  $-0.65$ , with compounds **4** and **1** observed to have the most positive and negative potentials, respectively. The overpotential is measured as the difference between the half-wave potential ( $E_{\text{cat}/2}$ ) of the catalytic wave [here: in a 1 mM (pH 3) aqueous solution] and the open-circuit potential of a platinum working electrode in the same solution under 1 atm of  $\text{H}_2$  pressure, because this has been determined in previous literature to be a systematic and accurate measure of a catalyst's performance (Figure S13).<sup>87,88</sup> This method provides an overpotential range of  $0.49$ – $0.57$  V versus platinum for our series of complexes on FTO/RGO electrodes. For the purpose of comparison, overpotential values determined by more dated methods using the onset potential of the catalytic wave range from  $0.3$  to  $0.5$  V versus platinum.<sup>89</sup>

All  $E_{\text{cat}/2}$  values are at least  $0.2$  V more negative than the  $E_{1/2}$  values observed in the absence of acid, indicating that reduction proceeds protonation in all cases during electrocatalytic proton reduction.

TFA titration CV studies for HOPG-adsorbed complexes in aqueous solutions yield similar results compared to those for the FTO/RGO electrodes, in all cases eliciting an increasing cathodic current response upon acid addition. The increase in the current response is linear with the acid concentration for all complexes with the exception of **5**, which undergoes a change in response similar to that observed for this compound on FTO/RGO (Figure S19). The resulting current response for **5** at higher acid concentrations is close to the HOPG background activity in potential and magnitude, suggesting desorption or decomposition of the complex. Interestingly, complex **6** exhibits

catalytic behavior consistent with complexes **1–4**, which contrasts with the inactivity/instability observed for this complex on FTO/RGO electrodes.

For complexes **2–4** and **6**, activity saturation is not observed even at and below pH values of 1.5, whereas **1** reaches its activity plateau at approximately 8 mM TFA (pH 2.1; see Figure 3). Catalytic rate estimates from CV data were determined using the ratio of the peak cathodic current in the presence/absence of acid and the catalyst surface coverage in eq 1, with the  $i_{\text{cat}}$  value at pH 1.5 used as a lower limit for activity for **2–4** and **6**. Here,  $A$  is the electrode surface area and  $\Gamma$  stands for the catalyst surface coverage on the electrode.

$$k_{\text{obs}} = \frac{i_{\text{cat}}}{nFA\Gamma} \quad (1)$$

This method provides a range of turnover frequency estimates from  $24 \text{ s}^{-1}$  for **6** to  $230 \text{ s}^{-1}$  for **2** (see Table 1), demonstrating that a vast difference in the activity is achievable by slight changes in the ligand substitution. On the basis of these estimates, the most active complexes for surface attachment are those with partial halide substitution in the ligand system.

Adding halide substituents to the benzenedithiolate complex (**1**), leading to the dichlorobenzenedithiolate derivative (**2**), causes a slight increase in  $k_{\text{obs}}$  from  $220$  to  $230 \text{ s}^{-1}$ ; further increasing the halide substitution in the tetrachlorobenzenedithiolate derivative (**3**) results in a substantial decrease in the estimated rate constant to  $120 \text{ s}^{-1}$ . A significant decrease is also observed when the tetrachloro-substituted (**3**) and tetrafluoro-substituted (**4**) derivatives are compared, with respective  $k_{\text{obs}}$  values of  $120$  and  $42 \text{ s}^{-1}$ . The size of the ligand ring system also has a dramatic effect on the estimated rate constant, leading to a decrease from  $220$  to  $24 \text{ s}^{-1}$  for the benzenedithiolate and naphthalenedithiolate derivatives, respectively. While these rate constant estimates provide insight into the effect of the ligand substitution on the molecular TOF, it is important to also note the change in the absolute observed activity, as better measured by  $i_{\text{cat}}$  without normalization to the catalyst surface coverage. One pertinent example is the comparison of **1** and **3**, in which the estimated rate of the latter is nearly half that of the former, but the peak catalytic current is, in fact, more than an order of magnitude higher for the tetrachloro derivative ( $i_{\text{cat}} = 224$  vs  $2818 \mu\text{A}$ ) due to the drastically higher catalyst loading for **3**. A similar result is observed for **1** and **6**, where the naphthalenedithiolate derivative has a peak catalytic current more than an order of magnitude higher than that of the benzenedithiolate derivative ( $2906$  and  $224 \mu\text{A}$ , respectively), despite having a 10-fold lower estimated rate. These enhancements in the  $i_{\text{cat}}$  values are a direct result of increasing the catalyst loading, as can most easily be seen in **6** compared to **1** [see Figures 3 (top) vs S22]. In summary, because the apparent activity observed for each catalyst is dependent on both the loading and TOF, the highest absolute activity ( $i_{\text{cat}}$ ) observed in the CV studies was not the derivative with the highest  $k_{\text{obs}}$  (**2**) or the highest loading (**6**) but rather the derivative with a moderate rate and loading (**3**). This is best illustrated by a direct comparison of the active catalyst derivatives on the same HOPG electrode under the same conditions (pH 2.4 in a TFA solution), as shown in Figure 4.

$E_{\text{cat}/2}$  values at pH 1.5 (or 2.1 in the case of **1**) range from  $-0.52$  to  $-0.71$ , with the most positive and negative potentials obtained for compounds **3** and **1**, respectively. The overpotential range calculated for the series on HOPG is  $0.44$ – $0.63$  V versus platinum, with generally good agreement (within  $0.05$

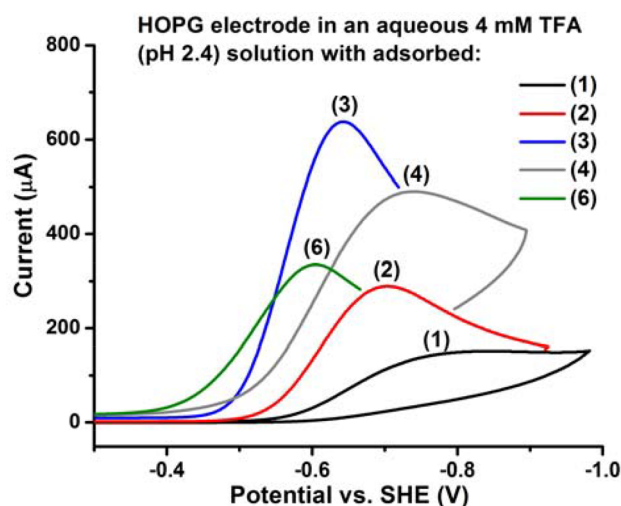


**Figure 4.** Cyclic voltammograms of active cobalt bis(benzenedithiolate) catalyst derivatives adsorbed on the same HOPG working electrode (after polishing) in an aqueous 0.1 M  $\text{KPF}_6$  solution with 4 mM TFA (pH 2.4). Platinum counter and Ag/AgCl reference electrodes are used, and potentials are reported versus SHE.

V) with the overpotential values on FTO/RGO (Table 1). The compounds exhibiting the lowest overpotentials were those with a high level of halide substitution, as in the case of 3 and 4 ( $\eta = 0.44$  V), and the one with a larger ligand ring system, complex 6 ( $\eta = 0.51$  V). On average,  $E_{\text{cat}/2}$  values are approximately 0.15 V more negative than the corresponding  $E_{1/2}$  values. As in the case of the FTO/RGO electrodes, the onset potentials are more negative than the  $E_{1/2}$  values, indicating that reduction precedes protonation in the electrocatalytic mechanism for proton reduction (an EC-type mechanism). This is in agreement with the mechanistic results by Eisenberg and co-workers, who showed that protonation of the formally cobalt(II) complex enables a further reduction that leads to dihydrogen generation.<sup>27</sup>

In summary, trends in the  $E_{\text{cat}/2}$  values are consistent across our series of complexes for both FTO/RGO and HOPG surfaces. Most significantly, upon an increase in the electron-withdrawing nature of the benzenedithiolate ligand, a decrease in  $k_{\text{obs}}$  is generally observed (with the exception of the dichloro derivative), while at the same time, the overpotential is lowered (which is the expected trend). A shift from an  $E_{\text{cat}/2}$  value of  $-0.65$  to  $-0.61$  and  $-0.58$  V is observed from 1 to 2 and then 3, respectively, on FTO/RGO electrodes, corresponding to 0, 2, and 4 chloro substitutions on each ligand. Similarly, on HOPG, a shift from  $-0.71$  to  $-0.67$  V and then  $-0.52$  V is observed from 1 to 3. Neither surface shows a significant difference in  $E_{\text{cat}/2}$  between the tetrachloro- and tetrafluoro-substituted ligand systems (3 and 4, respectively), with a 10 mV lower overpotential for 4 on FTO/RGO and nearly the opposite trend on HOPG. Extension of the ligand ring system from benzene to naphthalene induces a shift in  $E_{\text{cat}/2}$  from  $-0.71$  to  $-0.59$  V, which is notably similar to the shift observed with the ring halide substitution on going from 1 to 3 or 4.

**Bulk Electrolysis.** Controlled-potential electrolysis (CPE) studies were performed on an HOPG electrode after adsorbing the catalyst in the same manner as that used for the CV studies. For this purpose, the most active compounds from the CV studies described above were selected. These correspond to

complexes 2, 3, and 6, representing the highest activity and highest catalyst loading on the graphitic surfaces. In addition, complex 1 was included to serve as a reference point, allowing an improved understanding of the effect of halide substitution and increasing ligand ring size on the catalyst activity and retention under turnover conditions. Under an applied potential of  $-0.5$  V in a 0.5 M (pH 0.3) sulfuric acid solution, complex 3 drew an initial current density of approximately  $65 \text{ mA cm}^{-2}$ , where the background is notably only  $1 \text{ mA cm}^{-2}$ . The current density diminishes over the course of many hours, reaching a plateau current of approximately  $7 \text{ mA cm}^{-2}$  ( $\sim 11\%$  of the original activity) after approximately 8 h. This current density is maintained for the duration of the experiment spanning over 14 h, never returning to the background current level observed for bare HOPG (Figure 5). In addition, in situ

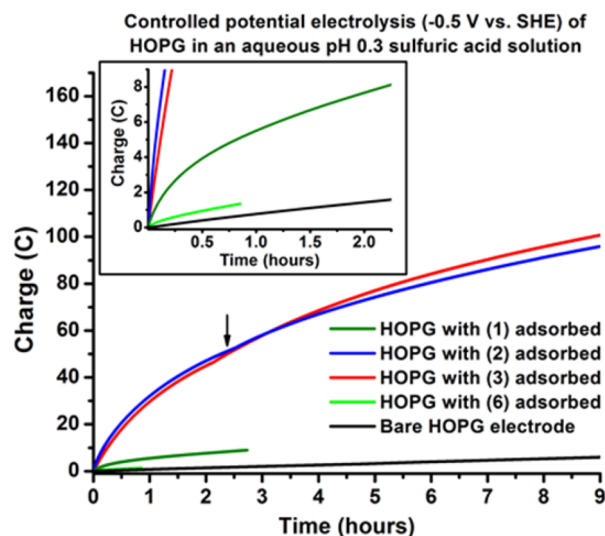


**Figure 5.** CPE at  $-0.5$  V versus SHE of several cobalt bis(dithiolene) catalyst derivatives adsorbed to the same HOPG electrode in an aqueous 0.1 M  $\text{KPF}_6$  solution with 0.5 M  $\text{H}_2\text{SO}_4$  (pH 0.3). A two-compartment cell is used with platinum counter and Ag/AgCl reference electrodes. The arrow indicates when the pH was adjusted back to 0.3. The inset provides a zoomed view to illustrate the limited stability of 6.

CV of the electrode after electrolysis, while showing substantially less current than before electrolysis, still exhibits notably more current drawn than a bare HOPG electrode (Figure S24).

Over the first 8 h of turnover for 3, a total of 96 C is passed by the catalyst-adsorbed HOPG electrode, while the same electrode without catalyst only passes 5 C in this time. To provide a TON for comparison, the initial active species is considered inactive after the plateau current is reached ( $\sim 8$  h). This corresponds to  $9.95 \times 10^{-4}$  mol of electrons passed and approximately  $5 \times 10^{-4}$  mol of dihydrogen formed based on a near-quantitative (97%) faradaic efficiency determined by gas chromatography analysis of dihydrogen formation over the first 5 h of CPE. From this value and an HOPG catalyst loading of  $1.24 \times 10^{-10}$  mol determined by CV quantification for 3, we can calculate a TON of  $4.02 \times 10^6$  over the 8 h period, as well as an average TOF of  $140 \text{ s}^{-1}$ . In contrast, the initial rate of the system is significantly higher, producing 18 C ( $9.33 \times 10^{-5}$  mol of dihydrogen) over the first 30 min to give a TOF of  $418 \text{ s}^{-1}$  under bulk electrolysis conditions.

Further analysis of the HOPG/3 system after CPE was conducted to ensure that the residual activity was not related to an uncontrolled cell variable or inaccuracy in the pH measurement. A separate HOPG electrode (never exposed to catalyst) was tested in the same solution and confirmed a definite difference in activity (Figure S24). Further analysis of the HOPG/3 system after electrolysis in a fresh, pH-neutral electrolyte solution showed a residual redox signal, albeit at a more negative potential ( $E_{1/2} = -0.55$  vs  $-0.35$  V initially) and with a much larger peak separation, indicative of a new species or altered electronic environment of the remaining surface-bound catalyst. Upon the addition of sulfuric acid to reach a pH of 1.5, a comparison of the HOPG/3 system with the control HOPG electrode by CV again showed substantially higher current levels than the background level, with an onset potential of approximately  $-0.45$  V for the catalytic wave. These results shown in Figure S25 confirm the presence of an active species that remains after electrolysis and which exhibits nearly 10 times lower current densities (at the previously applied potential) compared to the freshly prepared electrodes.

Complex 2 was observed to have behavior very similar to that of 3 under CPE conditions, with an initial current density of approximately  $65 \text{ mA cm}^{-2}$  and an initial TOF of  $835 \text{ s}^{-1}$  over the first 30 min. The current density is again seen to diminish over the course of many hours, reaching a plateau current of approximately  $6 \text{ mA cm}^{-2}$  ( $\sim 9\%$  original) after approximately 8 h. Over this time, 91 C are passed, corresponding to  $9.43 \times 10^{-4}$  mol of electrons passed and  $4.71 \times 10^{-4}$  mol of dihydrogen formed. From these data and an HOPG catalyst loading of  $5.18 \times 10^{-11}$  mol for 2, a TON of  $9.10 \times 10^6$  can be calculated for the 8 h period, with an average TOF of  $320 \text{ s}^{-1}$ .

Analysis of complex 6 under electrolysis conditions shows an initial current density of  $15 \text{ mA cm}^{-2}$ . Unlike in the case of complex 3, the current density decreases exponentially over the course of the first 10 min, reaching a plateau current consistent with background HOPG within less than an hour of electrolysis, indicating the complete loss of catalyst activity via desorption or catalyst degradation, in agreement with the CV results. After the plateau current was reached at  $t = \sim 30$  min, a total of 0.95 C had passed, corresponding to  $4.92 \times 10^{-6}$  mol of dihydrogen produced and a TON of  $7.90 \times 10^3$  based on a catalyst loading of  $6.22 \times 10^{-10}$  mol. An average TOF of  $4.4 \text{ s}^{-1}$  is determined for the 30 min, although it is important to note the relatively low rate combined with the short lifetime of the catalyst produced a significantly smaller amount of current compared to 3, so both TON and TOF estimates include some error and are higher-end estimates. Postelectrolysis analysis, performed analogously to complex 3, showed no substantial redox signal above the background in a fresh pH-neutral electrolyte solution, indicating no trace of 6 or a redox-active decomposition product present on the surface after electrolysis.

CPE of complex 1 shows intermediate behavior compared to that of the naphthalene and the halide-substituted derivatives. An initial current density of  $30 \text{ mA cm}^{-2}$  was observed, which also decreases more rapidly than that in the case of the halide derivatives, although the almost immediate plateau seen for 6 is not observed. A plateau current of less than 10% of the initial current was reached after approximately 1.5 h of electrolysis. At this time, a total of 6.7 C had passed, corresponding to  $3.47 \times 10^{-5}$  mol of dihydrogen produced and a TON of  $4.3 \times 10^6$  based on a catalyst loading of  $5.39 \times 10^{-12}$  mol. Despite the large TON, significantly less dihydrogen is produced for 1 per electrode area because of the much lower surface coverage

compared to 2 and 3. An average TOF of  $800 \text{ s}^{-1}$  is calculated for the first 1.5 h for 1.

## DISCUSSION

To design photoelectrodes and fuel-cell systems capable of efficiently interconverting simple chemical feedstocks into products that are useful as energy carriers or value-added industrial feedstocks (especially dihydrogen from water, methanol from carbon dioxide, etc.), it is a key challenge to design electrode surfaces with catalytic properties that can then act as heterogeneous catalysts in large-scale flow reactors. This can be accomplished either by developing solid-state electrode materials with catalytically active surfaces or by immobilizing a molecular catalyst on the electrode surface. With respect to the latter, we describe a new approach here where catalyst binding is only based on electrostatic interactions using a thin coating of RGO as the interface between the catalyst and a metal oxide electrode. This strategy provides substantial merits over other approaches in terms of simplicity and flexibility in application because RGO can be electrodeposited on almost any conductive material and, alternatively, can be produced by the chemical reduction of GO and then deposited on other substrates if necessary. The combination of versatility in substrate selection and the ability to easily tune molecular catalysts provides an opportunity to design nearly limitless systems in terms of activity and overpotential. This manuscript provides an example of such a system in which catalysts were easily prepared and functionalized to afford chemically tuned, highly active yet inexpensive, oxygen-stable heterogeneous catalyst systems functional in acidic aqueous media for proton reduction. In this way, this work highlights the advantage of using immobilized molecular catalysts for heterogeneous dihydrogen production systems over solid-state approaches because the overpotential, catalyst loading, and activity can all be directly controlled by simple ligand modifications in molecular systems. This is in contrast to solid-state catalysts, where catalytic sites often correspond to defect sites on the surface that are hard to identify, characterize, and systematically improve.

Characterization of our cobalt-catalyst-adsorbed FTO/RGO surfaces by XPS confirms the presence of a cobalt species with two distinct resonance states, which is a hallmark of cobalt bis(dithiolene) complexes.<sup>66,75,76</sup> In addition, XPS confirms the presence of thiol and chloride components. The Co and S 2p spectra are also consistent with the corresponding XPS signals observed for the polymeric analogues.<sup>67,68</sup> These results provide strong evidence that the species adsorbed to the surfaces are not cobalt nanoparticles or solid-state materials such as cobalt sulfide but rather molecular cobalt complexes that contain organic phenyl moieties as ligands. CV of the cobalt bis(benzenedithiolate) complexes on FTO/RGO and HOPG electrodes provides further insight into catalyst binding to these electrode surfaces. The consistently more negative  $E_{1/2}$  values observed for 1–6 on HOPG versus FTO/RGO electrodes suggest that the electronic interaction of the complexes with the surface is different for the two materials, which is reasonable considering the relative topography and surface groups present for edge-plane graphite versus RGO. More specifically, HOPG shows a regular  $sp^2$ -hybridized honeycomb lattice, whereas investigations on RGO films have revealed the presence of many  $\text{CO}_x$  moieties on the surface (alcohol, aldehyde, and carboxylate groups and epoxides) and substantially less  $sp^2$ -hybridized bonding character ( $\sim 70\%$  area)

but also significantly more disorder and the presence of substantially more holes ( $\sim 5\%$  area).<sup>90–93</sup> Variances in the peak separation and broadness of the current signals are commonly observed for  $E_{1/2}$  values in FTO/RGO/catalyst systems and can likely be attributed to the fact that each FTO/RGO-deposited surface varies significantly in topography and in surface  $\text{CO}_x$  speciation.<sup>92,93</sup> It is therefore advantageous to use the more homogeneous HOPG electrodes to quantitatively compare the catalytic activity of complexes 1–6. However, in terms of future applications, our FTO/RGO/catalyst system provides a design blueprint, along with catalyst activity profiles, of how other types of semiconductors could be surface-functionalized using an RGO interface.

A comparison of the catalyst loading on the same HOPG electrode for the various cobalt bis(benzenedithiolate) complexes investigated here provides an effective internal standard to determine the effect of ligand substitution on the surface adsorption and catalyst activity. A substantial increase in the catalyst loading is observed with the addition of halide substituents to the benzenedithiolate rings, at least for the chloro and fluoro derivatives studied here. In fact, whereas the CV signal of 1 is barely detectable above the non-Faradaic current, 2 shows a prominent signal an order of magnitude higher in integral intensity. A comparison of the naphthalene ligand system with the benzene derivative shows the largest increase in loading across the different ligand systems, effecting a change on the scale of over 2 orders of magnitude from the lowest observed loading in 1 to the highest in the series in 6. Notably, the estimates for 2 and 3 are comparable to those reported by Dey and co-workers ( $\sim 10^{-10}$  mol  $\text{cm}^{-2}$ ) for adsorption of diiron hydrogenase model complexes on similar EPG electrodes.<sup>24</sup>

The electrocatalytic responses of complexes 1–4 adsorbed on either FTO/RGO or HOPG are generally impressive, demonstrating the value of the RGO interface in allowing for fast electron transfer across the interface to a surface-immobilized catalyst, which promises the potential use of RGO in a variety of applications interfacing catalysts with semiconductor electrodes. A comparison of the catalytic behavior across our ligand series on a HOPG electrode provides insight into the effect of ligand substitution on the activity and overpotential. Most apparent is the trend for lower overpotential with higher halide substitution, as observed for complexes 1–3. Surprisingly, while the increase in halide substitution from 1 to 3 causes a decrease of more than 100 mV in the overpotential ( $\eta = 0.63$  vs  $0.44$  V), the effect of tetrafluoro substitution in 4 compared to tetrachloro substitution in 3 on the overpotential is seemingly unbeneficial ( $\eta = 0.46$  vs  $0.44$  V). A possible explanation for this surprising result is the change in the thiolate basicity: after reduction to cobalt(II), the catalyst is protonated (must be at the thiolate ligand, which is the only basic site) before reduction to cobalt(I) occurs. So, at low pH, there is likely a PCET process occurring, and while the electron-withdrawing substituents help with the cobalt(III)/cobalt(II) reduction potential, they also reduce the basicity of the thiolate ligand. This is a possible explanation that, however, requires further study. The overpotential also decreases significantly from 1 to 6 ( $\eta = 0.63$  vs  $0.51$  V), likely because of the enhanced electron delocalization and the somewhat electron-withdrawing properties of the larger aromatic ring system. The peak catalytic current ( $i_{\text{cat}}$ ) values are seen to follow a similar pattern, with over a 10-fold increase from 1 to 3 resulting from increased halide substitution of the

ligand. This increase is to a large degree caused by the sequential increase in the catalyst loading from 1 to 3; this is particularly true in the case of 1, which has the second highest molecular rate of all of the derivatives but suffers from a substantially lower loading. So, from a practical point of view, catalysts 2 and 3 are the champions, leading to the largest amount of dihydrogen produced per electrode surface area. The increased ring system size in 6 also results in a decrease in  $k_{\text{obs}}$  compared to 1. In fact, despite the large catalyst loading in 6, this complex is observed to have the lowest catalytic activity for proton reduction of all of the derivatives tested. On the basis of all of these considerations, catalyst 3 is the overall champion in terms of the peak catalytic current, overpotential under application conditions, and stability on graphitic surfaces. Catalyst 2 provides close competition, boasting a superior rate from CV studies and only slightly lower retention under turnover conditions. Additionally, 2 shines because of its ease of preparation (the ligand is commercially available).

Analysis of complexes 1–6 adsorbed on HOPG allows for observation of the catalysts in direct comparison at higher acid concentrations (low pH conditions), revealing an impressive activity level for dihydrogen production ( $k_{\text{obs}}$  values of  $24$ – $230$   $\text{s}^{-1}$  at pH 1.5). The catalyst-adsorbed electrodes typically reach current densities of  $10$   $\text{mA cm}^{-2}$  at pH 1.5 with potentials lower than  $-0.5$  V versus RHE, and 2 and 3 can attain current densities higher than  $60$   $\text{mA cm}^{-2}$  at pH 0.3 with an applied potential of only  $-0.48$  V versus RHE. Electrocatalytic behavior of the cobalt complexes is overall very similar on the HOPG and FTO/RGO electrodes. Key features include a linear response of the current with increasing acid concentration, a lack of activity saturation even at higher acid concentrations, and catalytic current onset potentials that typically occur at a more negative potential than the observed  $E_{1/2}$ .

The TOF values observed during long-term electrolysis, in particular the initial rates of 1–3, are higher than the CV estimates determined by eq 1. This suggests that the CV quantification method can provide a rough estimate of the catalytic activity but may not generally be accurate for real application conditions. It is therefore particularly important that new proton reduction catalysts are tested under bulk electrolysis conditions to obtain a realistic measure of their true electrocatalytic activity and, in particular, stability. Sustained activity above the background current for 2 and 3 after the initial 8 h suggests that either a small percentage of the catalyst remains active indefinitely or a more stable, less active species is formed under turnover conditions after the first 6–8 h. These results are particularly interesting in comparison to our previous studies on bulk (not highly ordered) graphite, which show no Co 2p signal by XPS after the plateau current is reached in analogous electrolysis studies.<sup>86</sup> A similar result is obtained here for 2 (see Figure S4). This suggests that either some catalyst remains on the surface (below XPS detection limit) or some other active species forms on both the bulk graphite and HOPG electrodes over time. The possibility of a nonmetallic active species can also not be excluded. This point requires further study.

The TOF observed here for 3 is comparable to those reported for surface-immobilized diiron hydrogenase models by Dey and co-workers (adsorbed on similar EPG electrodes and tested under identical conditions). Dey's system is reported to have an overpotential of  $0.18$  V versus the thermodynamic limit of proton reduction for a pH 3  $\text{H}_2\text{SO}_4$  solution. Under identical CPE conditions, the catalyst-adsorbed EPG disks

produce  $\sim 5.5 \times 10^{-4}$  mol of dihydrogen (vs  $\sim 5 \times 10^{-4}$  mol obtained here for **3**) in the same time frame with a similar loading ( $6.22 \times 10^{-10}$  mol  $\text{cm}^{-2}$  for **3** vs  $\sim 10^{-10}$  mol  $\text{cm}^{-2}$  for Dey's catalyst). This ranks our heterogeneous systems among those with the highest molecular TOFs reported so far in the literature.<sup>24,36,94,95</sup>

The disparity in the lifetime on HOPG under CPE observed for the halide-substituted catalyst derivatives (**2** and **3**) and the derivatives with an unsubstituted ring system (**1** and **6**) is substantial, with complete loss of activity for both **1** and **6** in less than 2 h, while the current density slowly decreases for **2** and **3** over approximately 8 h. *These results indicate an inherent difference in the ligand properties that promote the initial adsorption and those that promote catalyst retention under turnover conditions.* This suggests that larger aromatic ring systems, such as those in **6**, are beneficial for adsorption onto graphitic surfaces, while more electron-poor ring systems, such as those used for **2** and **3**, are less prone to desorption during turnover. This is a very interesting finding with respect to the further optimization of our cobalt catalysts for heterogeneous electrocatalytic proton reduction in the future.

In addition to closely matching the XPS spectra, the graphite-adsorbed cobalt bis(benzenedithiolate) systems reported here show very similar electrocatalytic characteristics compared to the polymeric forms of these molecules reported by Marinescu and co-workers.<sup>67,68</sup> Onset potentials of approximately  $-0.44$  V for **3** and **6** on HOPG at pH 1.3 are very similar to those reported for the two-dimensional ( $-0.28$  V) and one-dimensional ( $\sim -0.45$  V) polymer materials. A current density of  $10 \text{ mA cm}^{-2}$  is reached by **3** at a potential of  $-0.56$  V versus SHE ( $-0.48$  V vs RHE) at pH 1.3 (Figure 6), compared to

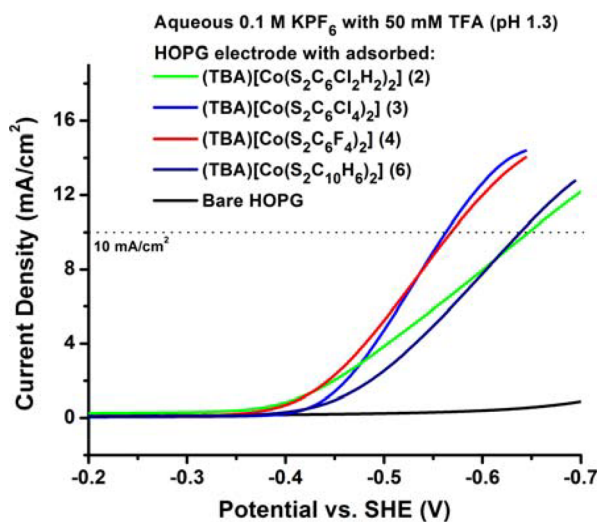


**Figure 6.** Polarization curves of active cobalt bis(benzenedithiolate) catalyst derivatives adsorbed on the same HOPG working electrode in an aqueous 0.1 M  $\text{KPF}_6$  solution with 50 mM TFA (pH 1.3). Platinum counter and  $\text{Ag}/\text{AgCl}$  reference electrodes were used, and potentials are reported versus SHE.

$-0.34$  V versus RHE reported for the two-dimensional MOSI on glassy carbon and  $-0.56$  V versus RHE reported for the one-dimensional polymer on glassy carbon. The current density of **3** is particularly impressive given that the catalyst loading is approximately 3–4 orders of magnitude lower than that reported for the polymer systems, while still reaching the  $10 \text{ mA cm}^{-2}$  threshold at similar potentials. This implies that the

molecular catalyst **3** is either 3–4 orders of magnitude more active than the polymeric catalysts or that the polymeric materials form stacked layers on the surface, where only the top layer(s) is/are catalytically active.

Finally, comparison should be made to nickel bis(diphosphine) dihydrogen production catalysts with pendant amine side chains, which represent the gold standard for proton reduction electrocatalysis in the homogeneous phase.<sup>4,19</sup> Nickel bis(diphosphine) complexes containing pendant amines covalently bound to indium–tin oxide-supported multiwalled carbon nanotubes (ITO/MWCNTs) reported by Le Goff and co-workers display a catalyst loading similar to that of **6** ( $\sim 1.5 \times 10^{-9}$  vs  $3.1 \times 10^{-9}$  mol  $\text{cm}^{-2}$ ). The covalently bound catalysts require an exceptionally low overpotential of 20 mV in aqueous media. CPE of the catalyst-bound ITO/MWCNT systems in an aqueous pH 0.3 solution at a potential of  $-0.3$  V versus SHE shows impressive stability with no decrease in the current density over a 10 h period and quantitative faradaic efficiency. However, the TOF determined from these experiments is somewhat low at  $7 \times 10^{-5} \text{ s}^{-1}$  ( $\sim 100000$  turnovers in 10 h), and a current density of only  $4 \text{ mA cm}^{-2}$  is observed at  $-0.3$  V versus SHE at pH 0.3.<sup>47</sup> A similar system reported by Tran and co-workers shows a similarly low average TOF of  $8.2 \text{ s}^{-1}$  ( $8.5 \times 10^4$  turnovers in 6 h with a catalyst loading of  $\sim 2 \times 10^{-9}$  mol<sub>cat</sub>  $\text{cm}^{-2}$ ).<sup>46</sup> Excitingly, the overall catalytic properties of the surface-immobilized cobalt complexes described in this paper therefore rival those of the best immobilized molecular catalyst systems reported to date.

## CONCLUSIONS

In this work, a series of cobalt bis(benzenedithiolate) derivatives has been prepared and adsorbed on graphitic surfaces to create heterogeneous electrocatalysts for efficient proton reduction. These systems exhibit excellent catalytic performance for dihydrogen production in moderately acidic aqueous solutions. These catalysts are simple and inexpensive to prepare and air-stable and can easily be adsorbed onto graphitic surfaces using a small amount of catalyst material in as little as 12 h. The catalyst loading increases as more electron-withdrawing substituents are added to the ligand, although an even stronger effect is seen as the size of the aromatic ring system increases. The overpotential decreases with increasing halide substitution of the benzenedithiolate ligand, although the differences observed between chloro and fluoro substituents are small. The inductive effect of the extended ring system is also seen to decrease the overpotential to a similar extent as the halide substituents. Activity trends are evident across the ligand series because turnover frequencies generally decrease with increasing halide substitution compared to the unsubstituted compound **1**. Under turnover conditions, halide-substituted derivatives slowly decrease in activity over the course of  $\sim 8$  h, while naphthalene derivatives rapidly deactivate within an hour, despite higher initial catalyst loading. Total turnovers of  $\sim 10^7$  in 8 h are accomplished in CPE experiments under real application conditions, with an average TOF of up to  $320 \text{ s}^{-1}$  over the 8 h period for the dichloro-substituted catalyst.

## ASSOCIATED CONTENT

### Supporting Information

The Supporting Information is available free of charge on the ACS Publications website at DOI: [10.1021/acs.inorgchem.7b01589](https://doi.org/10.1021/acs.inorgchem.7b01589).

Index of figures, details for overpotential and rate constant calculations, and full crystallographic data sets (PDF)

### Accession Codes

CCDC 1557448 contains the supplementary crystallographic data for this paper. These data can be obtained free of charge via [www.ccdc.cam.ac.uk/data\\_request/cif](http://www.ccdc.cam.ac.uk/data_request/cif), or by emailing [data\\_request@ccdc.cam.ac.uk](mailto:data_request@ccdc.cam.ac.uk), or by contacting The Cambridge Crystallographic Data Centre, 12 Union Road, Cambridge CB2 1EZ, UK; fax: +44 1223 336033.

### AUTHOR INFORMATION

#### Corresponding Author

\*E-mail: [lehnrtn@umich.edu](mailto:lehnrtn@umich.edu) (N.L.).

#### ORCID

Nicolai Lehnert: 0000-0002-5221-5498

#### Author Contributions

The manuscript was written through contributions of all authors. All authors have given approval to the final version of the manuscript.

#### Notes

The authors declare no competing financial interest.

### ACKNOWLEDGMENTS

N.L. acknowledges funding from 3M (Grant NTFG 5286067) for this work. Further support to S.C.E. was provided by the Rackham Graduate School (University of Michigan). Acknowledgement is also made for funding from NSF Grants CHE-0840456, DMR-0420785, and DMR-0320740 for X-ray crystallography, XPS, and scanning electron microscopy instrumentation, respectively.

### REFERENCES

- (1) Nocera, D. G. The Artificial Leaf. *Acc. Chem. Res.* **2012**, *45*, 767–776.
- (2) Dempsey, J. L.; Brunschwig, B. S.; Winkler, J. R.; Gray, H. B. Hydrogen Evolution Catalyzed by Cobaloximes. *Acc. Chem. Res.* **2009**, *42*, 1995–2004.
- (3) Kim, D.; Sakimoto, K. K.; Hong, D.; Yang, P. Artificial Photosynthesis for Sustainable Fuel and Chemical Production. *Angew. Chem., Int. Ed.* **2015**, *54*, 3259–3266.
- (4) Rakowski DuBois, M.; DuBois, D. L. Development of Molecular Electrocatalysts for CO<sub>2</sub> Reduction and H<sub>2</sub> Production/Oxidation. *Acc. Chem. Res.* **2009**, *42*, 1974–1982.
- (5) Stolley, R. M.; Helm, M. L. Light-harvesting materials: Soft support for energy conversion. *Nat. Chem.* **2014**, *6*, 949–950.
- (6) Artero, V.; Chavarot-Kerlidou, M.; Fontecave, M. Splitting Water with Cobalt. *Angew. Chem., Int. Ed.* **2011**, *50*, 7238–7266.
- (7) Savéant, J.-M. Molecular Catalysis of Electrochemical Reactions. Mechanistic Aspects. *Chem. Rev.* **2008**, *108*, 2348–2378.
- (8) Walter, M. G.; Warren, E. L.; McKone, J. R.; Boettcher, S. W.; Mi, Q.; Santori, E. A.; Lewis, N. S. Solar Water Splitting Cells. *Chem. Rev.* **2010**, *110*, 6446–6473.
- (9) Valdez, C. N.; Dempsey, J. L.; Brunschwig, B. S.; Winkler, J. R.; Gray, H. B. Catalytic hydrogen evolution from a covalently linked dicobaloxime. *Proc. Natl. Acad. Sci. U. S. A.* **2012**, *109*, 15589–15593.
- (10) Sala, X.; Romero, I.; Rodríguez, M.; Escriche, L.; Llobet, A. Molecular Catalysts that Oxidize Water to Dioxygen. *Angew. Chem., Int. Ed.* **2009**, *48*, 2842–2852.
- (11) Beyler, M.; Ezzaher, S.; Karnahl, M.; Santoni, M.-P.; Lomoth, R.; Ott, S. Pentacoordinate iron complexes as functional models of the distal iron in [FeFe] hydrogenases. *Chem. Commun.* **2011**, *47*, 11662–11664.
- (12) Canaguier, S.; Artero, V.; Fontecave, M. Modelling NiFe hydrogenases: nickel-based electrocatalysts for hydrogen production. *J. Chem. Soc., Dalton Trans.* **2008**, 315–325.
- (13) Capon, J.-F.; Ezzaher, S.; Gloaguen, F.; Pétilion, F. Y.; Schollhammer, P.; Talarmin, J. Electrochemical Insights into the Mechanisms of Proton Reduction by [Fe<sub>2</sub>(CO)<sub>6</sub>{μ-SCH<sub>2</sub>N(R)-CH<sub>2</sub>S}] Complexes Related to the [2Fe]<sub>H</sub> Subsite of [FeFe]-Hydrogenase. *Chem. - Eur. J.* **2008**, *14*, 1954–1964.
- (14) Baffert, C.; Artero, V.; Fontecave, M. Cobaloximes as Functional Models for Hydrogenases. 2. Proton Electroreduction Catalyzed by Difluoroborylbis(dimethylglyoximate)cobalt(II) Complexes in Organic Media. *Inorg. Chem.* **2007**, *46*, 1817–1824.
- (15) Yu, Z.; Wang, M.; Li, P.; Dong, W.; Wang, F.; Sun, L. Diiron dithiolate complexes containing intra-ligand NH...S hydrogen bonds: [FeFe] hydrogenase active site models for the electrochemical proton reduction of HOAc with low overpotential. *J. Chem. Soc., Dalton Trans.* **2008**, 2400–2406.
- (16) Roy, S.; Mazinani, S. K. S.; Groy, T. L.; Gan, L.; Tarakeshwar, P.; Mujica, V.; Jones, A. K. Catalytic Hydrogen Evolution by Fe(II) Carbonyls Featuring a Dithiolate and a Chelating Phosphine. *Inorg. Chem.* **2014**, *53*, 8919–8929.
- (17) McKone, J. R.; Marinescu, S. C.; Brunschwig, B. S.; Winkler, J. R.; Gray, H. B. Earth-abundant hydrogen evolution electrocatalysts. *Chem. Sci.* **2014**, *5*, 865–878.
- (18) Wang, M.; Chen, L.; Sun, L. Recent progress in electrochemical hydrogen production with earth-abundant metal complexes as catalysts. *Energy Environ. Sci.* **2012**, *5*, 6763–6778.
- (19) Helm, M. L.; Stewart, M. P.; Bullock, R. M.; DuBois, M. R.; DuBois, D. L. A Synthetic Nickel Electrocatalyst with a Turnover Frequency Above 100,000 s<sup>-1</sup> for H<sub>2</sub> Production. *Science* **2011**, *333*, 863–866.
- (20) Losse, S.; Vos, J. G.; Rau, S. Catalytic hydrogen production at cobalt centres. *Coord. Chem. Rev.* **2010**, *254*, 2492–2504.
- (21) Tard, C.; Pickett, C. J. Structural and Functional Analogues of the Active Sites of the [Fe]-, [NiFe]-, and [FeFe]-Hydrogenases. *Chem. Rev.* **2009**, *109*, 2245–2274.
- (22) Stewart, M. P.; Ho, M.-H.; Wiese, S.; Lindstrom, M. L.; Thogerson, C. E.; Raugei, S.; Bullock, R. M.; Helm, M. L. High Catalytic Rates for Hydrogen Production Using Nickel Electrocatalysts with Seven-Membered Cyclic Diphosphine Ligands Containing One Pendant Amine. *J. Am. Chem. Soc.* **2013**, *135*, 6033–6046.
- (23) Eckenhoff, W. T.; Eisenberg, R. Molecular systems for light driven hydrogen production. *Dalton Trans.* **2012**, *41*, 13004–13021.
- (24) Dey, S.; Rana, A.; Dey, S. G.; Dey, A. Electrochemical Hydrogen Production in Acidic Water by an Azadithiolate Bridged Synthetic Hydrogenase Mimic: Role of Aqueous Solvation in Lowering Overpotential. *ACS Catal.* **2013**, *3*, 429–436.
- (25) Eckenhoff, W. T.; McNamara, W. R.; Du, P.; Eisenberg, R. Cobalt complexes as artificial hydrogenases for the reductive side of water splitting. *Biochim. Biophys. Acta, Bioenerg.* **2013**, *1827*, 958–973.
- (26) McNamara, W. R.; Han, Z.; Alperin, P. J.; Brennessel, W. W.; Holland, P. L.; Eisenberg, R. A CobaltDithiolene Complex for the Photocatalytic and Electrocatalytic Reduction of Protons. *J. Am. Chem. Soc.* **2011**, *133*, 15368–15371.
- (27) McNamara, W. R.; Han, Z.; Yin, C. J.; Brennessel, W. W.; Holland, P. L.; Eisenberg, R. Cobalt-dithiolene complexes for the photocatalytic and electrocatalytic reduction of protons in aqueous solutions. *Proc. Natl. Acad. Sci. U. S. A.* **2012**, *109*, 15594–15599.
- (28) Lakadamyali, F.; Kato, M.; Muresan, N. M.; Reiser, E. Selective Reduction of Aqueous Protons to Hydrogen with a Synthetic Cobaloxime Catalyst in the Presence of Atmospheric Oxygen. *Angew. Chem., Int. Ed.* **2012**, *51*, 9381–9384.
- (29) Gao, W.; Ekström, J.; Liu, J.; Chen, C.; Eriksson, L.; Weng, L.; Åkermark, B.; Sun, L. Binuclear Iron-Sulfur Complexes with Bidentate Phosphine Ligands as Active Site Models of Fe-Hydrogenase and Their Catalytic Proton Reduction. *Inorg. Chem.* **2007**, *46*, 1981–1991.
- (30) Duan, L.; Wang, M.; Li, P.; Na, Y.; Wang, N.; Sun, L. Carbene-pyridine chelating 2Fe2S hydrogenase model complexes as highly

active catalysts for the electrochemical reduction of protons from weak acid (HOAc). *J. Chem. Soc., Dalton Trans.* **2007**, 1277–1283.

(31) Cheah, M. H.; Tard, C.; Borg, S. J.; Liu, X.; Ibrahim, S. K.; Pickett, C. J.; Best, S. P. Modeling [Fe-Fe] Hydrogenase: Evidence for Bridging Carbonyl and Distal Iron Coordination Vacancy in an Electrocatalytically Competent Proton Reduction by an Iron Thiolate Assembly That Operates through Fe(0)-Fe(II) Levels. *J. Am. Chem. Soc.* **2007**, *129*, 11085–11092.

(32) Bigi, J. P.; Hanna, T. E.; Harman, W. H.; Chang, A.; Chang, C. J. Electrocatalytic reduction of protons to hydrogen by a water-compatible cobalt polypyridyl platform. *Chem. Commun.* **2010**, *46*, 958–960.

(33) Pantani, O.; Naskar, S.; Guillot, R.; Millet, P.; Anxolabéhère-Mallart, E.; Aukauloo, A. Cobalt Clathrochelate Complexes as Hydrogen-Producing Catalysts. *Angew. Chem., Int. Ed.* **2008**, *47*, 9948–9950.

(34) McCrory, C. C. L.; Uyeda, C.; Peters, J. C. Electrocatalytic Hydrogen Evolution in Acidic Water with Molecular Cobalt Tetraazamacrocycles. *J. Am. Chem. Soc.* **2012**, *134*, 3164–3170.

(35) Hu, X.; Brunschwig, B. S.; Peters, J. C. Electrocatalytic Hydrogen Evolution at Low Overpotentials by Cobalt Macrocyclic Glyoxime and Tetraimine Complexes. *J. Am. Chem. Soc.* **2007**, *129*, 8988–8998.

(36) Berben, L. A.; Peters, J. C. Hydrogen evolution by cobalt tetraimine catalysts adsorbed on electrode surfaces. *Chem. Commun.* **2010**, *46*, 398–400.

(37) Andreiadis, E. S.; Jacques, P.-A.; Tran, P. D.; Leyris, A.; Chavarot-Kerlidou, M.; Joussetme, B.; Matheron, M.; Pecaut, J.; Palacin, S.; Fontecave, M.; Artero, V. Molecular engineering of a cobalt-based electrocatalytic nanomaterial for H<sub>2</sub> evolution under fully aqueous conditions. *Nat. Chem.* **2012**, *5*, 48–53.

(38) Carroll, M. E.; Barton, B. E.; Gray, D. L.; Mack, A. E.; Rauchfuss, T. B. Active-Site Models for the Nickel–Iron Hydrogenases: Effects of Ligands on Reactivity and Catalytic Properties. *Inorg. Chem.* **2011**, *50*, 9554–9563.

(39) Gärtner, F.; Boddien, A.; Barsch, E.; Fumino, K.; Losse, S.; Junge, H.; Hollmann, D.; Brückner, A.; Ludwig, R.; Beller, M. Photocatalytic Hydrogen Generation from Water with Iron Carbonyl Phosphine Complexes: Improved Water Reduction Catalysts and Mechanistic Insights. *Chem. - Eur. J.* **2011**, *17*, 6425–6436.

(40) Ott, S.; Kritikos, M.; Åkermark, B.; Sun, L. Synthesis and Structure of a Biomimetic Model of the Iron Hydrogenase Active Site Covalently Linked to a Ruthenium Photosensitizer. *Angew. Chem., Int. Ed.* **2003**, *42*, 3285–3288.

(41) Wiedner, E. S.; Yang, J. Y.; Dougherty, W. G.; Kassel, W. S.; Bullock, R. M.; DuBois, M. R.; DuBois, D. L. Comparison of Cobalt and Nickel Complexes with Sterically Demanding Cyclic Diphosphine Ligands: Electrocatalytic H<sub>2</sub> Production by [Co(PtBu<sub>2</sub>NPh<sub>2</sub>)-(CH<sub>3</sub>CN)<sub>3</sub>](BF<sub>4</sub>)<sub>2</sub>. *Organometallics* **2010**, *29*, 5390–5401.

(42) Orthaber, A.; Karnahl, M.; Tschierlei, S.; Streich, D.; Stein, M.; Ott, S. Coordination and conformational isomers in mononuclear iron complexes with pertinence to the [FeFe] hydrogenase active site. *Dalton Trans.* **2014**, *43*, 4537–4549.

(43) Eady, S. C.; Breault, T.; Thompson, L.; Lehnert, N. Highly functionalizable penta-coordinate iron hydrogen production catalysts with low overpotentials. *Dalton Trans.* **2016**, *45*, 1138–1151.

(44) Ibrahim, S. K.; Liu, X.; Tard, C.; Pickett, C. J. Electropolymeric materials incorporating subsite structures related to iron-only hydrogenase: active ester functionalised poly(pyrrroles) for covalent binding of {2Fe3S}-carbonyl/cyanide assemblies. *Chem. Commun.* **2007**, 1535–1537.

(45) Chiou, T.-W.; Lu, T.-T.; Wu, Y.-H.; Yu, Y.-J.; Chu, L.-K.; Liaw, W.-F. Development of a Dinitrosyl Iron Complex Molecular Catalyst into a Hydrogen Evolution Cathode. *Angew. Chem., Int. Ed.* **2015**, *54*, 14824–14829.

(46) Tran, P. D.; Le Goff, A.; Heidkamp, J.; Joussetme, B.; Guillet, N.; Palacin, S.; Dau, H.; Fontecave, M.; Artero, V. Noncovalent Modification of Carbon Nanotubes with Pyrene-Functionalized Nickel

Complexes: Carbon Monoxide Tolerant Catalysts for Hydrogen Evolution and Uptake. *Angew. Chem., Int. Ed.* **2011**, *50*, 1371–1374.

(47) Le Goff, A.; Artero, V.; Joussetme, B.; Tran, P. D.; Guillet, N.; Métayé, R.; Fihri, A.; Palacin, S.; Fontecave, M. From Hydrogenases to Noble Metal-Free Catalytic Nanomaterials for H<sub>2</sub> Production and Uptake. *Science* **2009**, *326*, 1384–1387.

(48) Krawicz, A.; Yang, J.; Anzenberg, E.; Yano, J.; Sharp, I. D.; Moore, G. F. Photofunctional Construct That Interfaces Molecular Cobalt-Based Catalysts for H<sub>2</sub> Production to a Visible-Light-Absorbing Semiconductor. *J. Am. Chem. Soc.* **2013**, *135*, 11861–11868.

(49) Seo, J.; Pekarek, R. T.; Rose, M. J. Photoelectrochemical operation of a surface-bound, nickel-phosphine H<sub>2</sub> evolution catalyst on p-Si(111): a molecular semiconductor/catalyst construct. *Chem. Commun.* **2015**, *51*, 13264–13267.

(50) Rao, H.; Wang, Z.-Y.; Zheng, H.-Q.; Wang, X.-B.; Pan, C.-M.; Fan, Y.-T.; Hou, H.-W. Photocatalytic hydrogen evolution from a cobalt/nickel complex with dithiolene ligands under irradiation with visible light. *Catal. Sci. Technol.* **2015**, *5*, 2332–2339.

(51) Fei, H.; Dong, J.; Arellano-Jimenez, M. J.; Ye, G.; Dong Kim, N.; Samuel, E. L. G.; Peng, Z.; Zhu, Z.; Qin, F.; Bao, J.; Yacamán, M. J.; Ajayan, P. M.; Chen, D.; Tour, J. M. Atomic cobalt on nitrogen-doped graphene for hydrogen generation. *Nat. Commun.* **2015**, *6*, 8668.

(52) Bullock, R. M.; Appel, A. M.; Helm, M. L. Production of hydrogen by electrocatalysis: making the H-H bond by combining protons and hydrides. *Chem. Commun.* **2014**, *50*, 3125–3143.

(53) Cardenas, A. J. P.; Ginovska, B.; Kumar, N.; Hou, J.; Raugei, S.; Helm, M. L.; Appel, A. M.; Bullock, R. M.; O'Hagan, M. Controlling Proton Delivery through Catalyst Structural Dynamics. *Angew. Chem., Int. Ed.* **2016**, *55*, 13509–13513.

(54) Stolley, R. M.; Darmon, J. M.; Das, P.; Helm, M. L. Nickel Bis-Diphosphine Complexes: Controlling the Binding and Heterolysis of H<sub>2</sub>. *Organometallics* **2016**, *35*, 2965–2974.

(55) Reback, M. L.; Buchko, G. W.; Kier, B. L.; Ginovska-Pangovska, B.; Xiong, Y.; Lense, S.; Hou, J.; Roberts, J. A. S.; Sorensen, C. M.; Raugei, S.; Squier, T. C.; Shaw, W. J. Enzyme Design from the Bottom Up: An Active Nickel Electrocatalyst with a Structured Peptide Outer Coordination Sphere. *Chem. - Eur. J.* **2014**, *20*, 1510–1514.

(56) Zou, X.; Huang, X.; Goswami, A.; Silva, R.; Sathe, B. R.; Míkmeková, E.; Asefa, T. Cobalt-Embedded Nitrogen-Rich Carbon Nanotubes Efficiently Catalyze Hydrogen Evolution Reaction at All pH Values. *Angew. Chem.* **2014**, *126*, 4461–4465.

(57) Chen, W.-F.; Muckerman, J. T.; Fujita, E. Recent developments in transition metal carbides and nitrides as hydrogen evolution electrocatalysts. *Chem. Commun.* **2013**, *49*, 8896–8909.

(58) Hou, J.; Fang, M.; Cardenas, A. J. P.; Shaw, W. J.; Helm, M. L.; Bullock, R. M.; Roberts, J. A. S.; O'Hagan, M. Electrocatalytic H<sub>2</sub> production with a turnover frequency > 10<sup>7</sup> s<sup>-1</sup>: the medium provides an increase in rate but not overpotential. *Energy Environ. Sci.* **2014**, *7*, 4013–4017.

(59) Gao, M.-R.; Liang, J.-X.; Zheng, Y.-R.; Xu, Y.-F.; Jiang, J.; Gao, Q.; Li, J.; Yu, S.-H. An efficient molybdenum disulfide/cobalt diselenide hybrid catalyst for electrochemical hydrogen generation. *Nat. Commun.* **2015**, *6*, 5982.

(60) Yin, Y.; Han, J.; Zhang, Y.; Zhang, X.; Xu, P.; Yuan, Q.; Samad, L.; Wang, X.; Wang, Y.; Zhang, Z.; Zhang, P.; Cao, X.; Song, B.; Jin, S. Contributions of Phase, Sulfur Vacancies, and Edges to the Hydrogen Evolution Reaction Catalytic Activity of Porous Molybdenum Disulfide Nanosheets. *J. Am. Chem. Soc.* **2016**, *138*, 7965–7972.

(61) Lassalle-Kaiser, B.; Merki, D.; Vrabel, H.; Gul, S.; Yachandra, V. K.; Hu, X.; Yano, J. Evidence from in Situ X-ray Absorption Spectroscopy for the Involvement of Terminal Disulfide in the Reduction of Protons by an Amorphous Molybdenum Sulfide Electrocatalyst. *J. Am. Chem. Soc.* **2015**, *137*, 314–321.

(62) Karunadasa, H. I.; Montalvo, E.; Sun, Y.; Majda, M.; Long, J. R.; Chang, C. J. A Molecular MoS<sub>2</sub> Edge Site Mimic for Catalytic Hydrogen Generation. *Science* **2012**, *335*, 698–702.

(63) Yang, Y.; Fei, H.; Ruan, G.; Tour, J. M. Porous Cobalt-Based Thin Film as a Bifunctional Catalyst for Hydrogen Generation and Oxygen Generation. *Adv. Mater.* **2015**, *27*, 3175–3180.

- (64) Blakemore, J. D.; Gupta, A.; Warren, J. J.; Brunschwigg, B. S.; Gray, H. B. Noncovalent Immobilization of Electrocatalysts on Carbon Electrodes for Fuel Production. *J. Am. Chem. Soc.* **2013**, *135*, 18288–18291.
- (65) Baker-Hawkes, M. J.; Billig, E.; Gray, H. B. Characterization and Electronic Structures of Metal Complexes Containing Benzene-1,2-dithiolate and Related Ligands. *J. Am. Chem. Soc.* **1966**, *88*, 4870–4875.
- (66) Sproules, S.; Wieghardt, K. Dithiolene radicals: Sulfur K-edge X-ray absorption spectroscopy and Harry's intuition. *Coord. Chem. Rev.* **2011**, *255*, 837–860.
- (67) Downes, C. A.; Marinescu, S. C. Efficient Electrochemical and Photoelectrochemical H<sub>2</sub> Production from Water by a Cobalt Dithiolene One-Dimensional Metal–Organic Surface. *J. Am. Chem. Soc.* **2015**, *137*, 13740–13743.
- (68) Clough, A. J.; Yoo, J. W.; Mecklenburg, M. H.; Marinescu, S. C. Two-Dimensional Metal–Organic Surfaces for Efficient Hydrogen Evolution from Water. *J. Am. Chem. Soc.* **2015**, *137*, 118–121.
- (69) Letko, C. S.; Panetier, J. A.; Head-Gordon, M.; Tilley, T. D. Mechanism of the Electrocatalytic Reduction of Protons with Diaryldithiolene Cobalt Complexes. *J. Am. Chem. Soc.* **2014**, *136*, 9364–9376.
- (70) Seidel, W. W.; Hahn, F. E. Chelate complexes of cobalt(III) with bis(dithiolate) ligands: backbone influence on the electronic properties and the reactivity of the metal center. *J. Chem. Soc., Dalton Trans.* **1999**, 2237–2242.
- (71) Nomura, M.; Fujita-Takayama, C.; Yagisawa, T.; Sugiyama, T.; Kajitani, M. An organometallic dithiolene complex exhibiting electrochemically initiated hydrogen generation. *Dalton Trans.* **2013**, *42*, 4764–4767.
- (72) Seidel, W. W.; Hahn, F. E. Chances and Limits of the Coordination Chemistry with Bis(benzene-1,2-dithiolato) Ligands. *Bioinorg. Chem. Appl.* **2005**, *3*, 69–80.
- (73) Machata, P.; Herich, P.; Lušpai, K.; Bucinsky, L.; Šoralová, S.; Breza, M.; Kozisek, J.; Rapta, P. Redox Reactions of Nickel, Copper, and Cobalt Complexes with “Noninnocent” Dithiolate Ligands: Combined in Situ Spectroelectrochemical and Theoretical Study. *Organometallics* **2014**, *33*, 4846–4859.
- (74) Solis, B. H.; Hammes-Schiffer, S. Computational Study of Anomalous Reduction Potentials for Hydrogen Evolution Catalyzed by Cobalt Dithiolene Complexes. *J. Am. Chem. Soc.* **2012**, *134*, 15253–15256.
- (75) Eisenberg, R.; Gray, H. B. Noninnocence in Metal Complexes: A Dithiolene Dawn. *Inorg. Chem.* **2011**, *50*, 9741–9751.
- (76) Periyasamy, G.; Burton, N. A.; Hillier, I. H.; Vincent, M. A.; Disley, H.; McMaster, J.; Garner, C. D. The dithiolene ligand—‘innocent’ or ‘non-innocent’? A theoretical and experimental study of some cobalt-dithiolene complexes. *Faraday Discuss.* **2007**, *135*, 469–488.
- (77) Eady, S. C.; Peczonczyk, S. L.; Maldonado, S.; Lehnert, N. Facile heterogenization of a cobalt catalyst via graphene adsorption: robust and versatile dihydrogen production system. *Chem. Commun.* **2014**, *50*, 8065–8068.
- (78) Weingarten, A. S.; Kazantsev, R. V.; Palmer, L. C.; McClendon, M.; Koltonow, A. R.; Samuel, A. P. S.; Kiebal, D. J.; Wasielewski, M. R.; Stupp, S. I. Self-assembling hydrogel scaffolds for photocatalytic hydrogen production. *Nat. Chem.* **2014**, *6*, 964–970.
- (79) Hart, H.; Bashir-Hashemi, A.; Luo, J.; Meador, M. A. Iptycenes: Extended triptycenes. *Tetrahedron* **1986**, *42*, 1641–1654.
- (80) Testaferri, L.; Tiecco, M.; Tingoli, M.; Chianelli, D.; Montanucci, M. Simple Syntheses of Aryl Alkyl Thioethers and of Aromatic Thiols from Unactivated Aryl Halides and Efficient Methods for Selective Dealkylation of Aryl Alkyl Ethers and Thioethers. *Synthesis* **1983**, *1983*, 751–755.
- (81) Hummers, W. S.; Offeman, R. E. Preparation of Graphitic Oxide. *J. Am. Chem. Soc.* **1958**, *80*, 1339–1339.
- (82) Haber, J. A.; Lewis, N. S. Infrared and X-ray Photoelectron Spectroscopic Studies of the Reactions of Hydrogen-Terminated Crystalline Si(111) and Si(100) Surfaces with Br<sub>2</sub>, I<sub>2</sub>, and Ferrocenium in Alcohol Solvents. *J. Phys. Chem. B* **2002**, *106*, 3639–3656.
- (83) Lindberg, B. J.; Hamrin, K.; Johansson, G.; Gelius, U.; Fahlman, A.; Nordling, C.; Siegbahn, K. Molecular Spectroscopy by Means of ESCA II. Sulfur compounds. Correlation of electron binding energy with structure. *Phys. Scr.* **1970**, *1*, 286.
- (84) Peng, S.; Li, L.; Han, X.; Sun, W.; Srinivasan, M.; Mhaisalkar, S. G.; Cheng, F.; Yan, Q.; Chen, J.; Ramakrishna, S. Cobalt Sulfide Nanosheet/Graphene/Carbon Nanotube Nanocomposites as Flexible Electrodes for Hydrogen Evolution. *Angew. Chem.* **2014**, *126*, 12802–12807.
- (85) Clark, D. T.; Kilcast, D.; Musgrave, W. K. R. Molecular core binding energies for some monosubstituted benzenes, as determined by X-ray photoelectron spectroscopy. *J. Chem. Soc. D* **1971**, 516–518.
- (86) Eady, S. C.; MacInnes, M. M.; Lehnert, N. A Smorgasbord of Carbon: Electrochemical Analysis of Cobalt–Bis(benzenedithiolate) Complex Adsorption and Electrocatalytic Activity on Diverse Graphitic Supports. *ACS Appl. Mater. Interfaces* **2016**, *8*, 23624–23634; Correction: *ACS Appl. Mater. Interfaces* **2017**, *9*, 15898–15899.
- (87) Fourmond, V.; Jacques, P.-A.; Fontecave, M.; Artero, V. H<sub>2</sub> Evolution and Molecular Electrocatalysts: Determination of Overpotentials and Effect of Homoconjugation. *Inorg. Chem.* **2010**, *49*, 10338–10347.
- (88) Hoffert, W. A.; Roberts, J. A. S.; Morris Bullock, R.; Helm, M. L. Production of H<sub>2</sub> at fast rates using a nickel electrocatalyst in water-acetonitrile solutions. *Chem. Commun.* **2013**, *49*, 7767–7769.
- (89) Felton, G. A. N.; Glass, R. S.; Lichtenberger, D. L.; Evans, D. H. Iron-Only Hydrogenase Mimics. Thermodynamic Aspects of the Use of Electrochemistry to Evaluate Catalytic Efficiency for Hydrogen Generation. *Inorg. Chem.* **2006**, *45*, 9181–9184.
- (90) Park, S. I.; Quate, C. F. Tunneling microscopy of graphite in air. *Appl. Phys. Lett.* **1986**, *48*, 112–114.
- (91) Gwo, S.; Shih, C. K. Site-selective imaging in scanning tunneling microscopy of graphite: The nature of site asymmetry. *Phys. Rev. B: Condens. Matter Mater. Phys.* **1993**, *47*, 13059–13062.
- (92) Dreyer, D. R.; Park, S.; Bielawski, C. W.; Ruoff, R. S. The chemistry of graphene oxide. *Chem. Soc. Rev.* **2010**, *39*, 228–240.
- (93) Erickson, K.; Erni, R.; Lee, Z.; Alem, N.; Gannett, W.; Zettl, A. Determination of the Local Chemical Structure of Graphene Oxide and Reduced Graphene Oxide. *Adv. Mater.* **2010**, *22*, 4467–4472.
- (94) Karunadasa, H. I.; Chang, C. J.; Long, J. R. A molecular molybdenum-oxo catalyst for generating hydrogen from water. *Nature* **2010**, *464*, 1329–1333.
- (95) Quentel, F.; Passard, G.; Gloaguen, F. Electrochemical hydrogen production in aqueous micellar solution by a diiron benzenedithiolate complex relevant to [FeFe] hydrogenases. *Energy Environ. Sci.* **2012**, *5*, 7757–7761.